

Chapter 10

Corrosion by Carbon Dioxide

10.1 INTRODUCTION

When pure iron is reacted with CO₂ at high temperatures, oxide scaling kinetics are observed [1–6] to be at first linear, and finally parabolic. This reflects the high diffusion coefficient of iron in the principal reaction product, wüstite, and the relatively slow surface reactions (dissociation of CO₂ and incorporation of chemisorbed oxygen into the scale). When the scale is thin, solid-state diffusion is much faster than the surface reactions and linear kinetics result. As the scale thickens, diffusion slows and eventually becomes rate controlling.

In fact, corrosion of iron in CO₂ is more complicated, involving, in addition, carburisation of the metal beneath its oxide scale. For example, at 900°C, initially ferritic iron develops a subsurface layer of austenite as it dissolves carbon [7].

For heat-resisting alloys, protective oxide scale growth is much slower than surface CO₂ reactions, and accordingly, parabolic kinetics are expected. In the case of many chromia-forming alloys, however, corrosion in CO₂ can lead to a transition from slow ‘protective’ scale growth to rapid ‘breakaway’ corrosion. The nature of the problem is illustrated in Fig. 10.1, where an Fe-20Cr alloy is seen to react with oxygen at 650°C to form a thin, adherent, highly protective chromia scale. When reacted with CO₂ at the same temperature, this alloy develops nodules of iron-rich oxide, which enlarge with time and coalesce to form a continuous, nonprotective scale [8,9]. Corrosion by CO₂ also leads to carburisation of the alloy, as seen in Fig. 10.2.

This breakaway corrosion was first found in CO₂-cooled nuclear reactors and was studied in the 60s and 70s [10–14]. Work has continued on the topic because helium-cooled reactors are subject to the same form of attack [15], as a result of interaction between the gas and the reactor core. The topic of CO₂ corrosion has attracted renewed interest with the development of new technologies for reduced greenhouse gas emissions, such as oxyfuel combustion of coal, concentrated solar thermal power generation and fast nuclear reactors using supercritical CO₂ as primary coolant.

In oxyfuel combustion [16], coal is burnt in oxygen and recirculated flue gas rather than air to allow easier separation of CO₂ from the exit gas. The

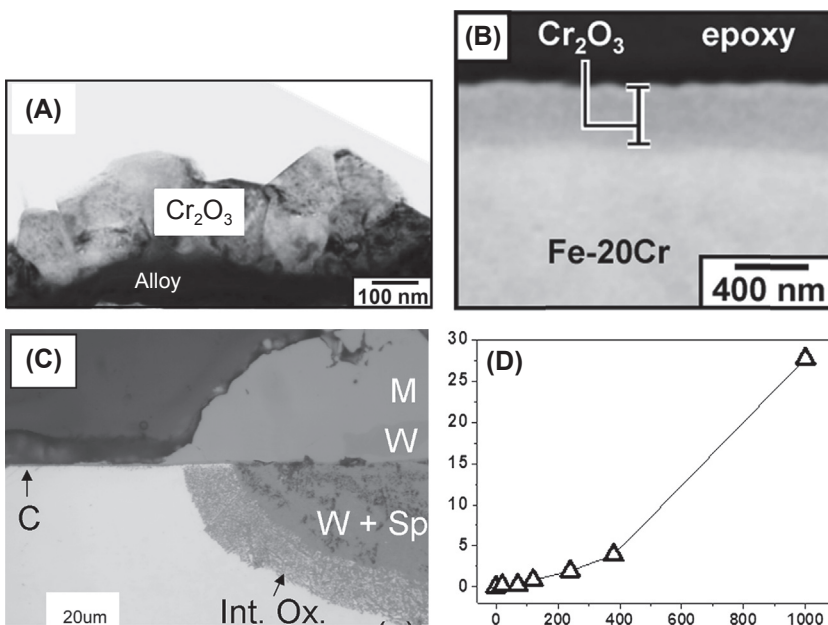


FIGURE 10.1 Cross-sections of Fe-20Cr reacted at 650°C: (A) in Ar-20O₂ for 24 h; (B and C) in Ar-20CO₂ for 20 and 240 h, respectively; (D) weight uptake kinetics. Phases marked in (C) are 'C' for chromia, 'M' for magnetite, 'W' for wüstite and 'Sp' for spinel.

combustion gas is consequently rich in CO₂ and H₂O(g). Laboratory experiments using CO₂-H₂O-rich atmospheres have shown them to be aggressively corrosive to chromium steels such as those used in boiler superheaters, as well as to model chromia-forming alloys.

Supercritical CO₂ has significant advantages as a heat transfer fluid and is being investigated for use in concentrated solar thermal power generation and

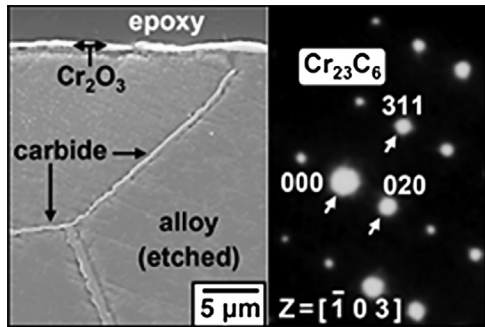


FIGURE 10.2 Alloy Fe-20Cr after reaction at 650°C for 120 h with Ar-20CO₂: SEM view of cross-section showing alloy grain boundary precipitates beneath external scale; SAD pattern identifies precipitates as Cr_{23}C_6 .

in fast nuclear reactors. In addition, the transport and storage of CO₂ captured from power generation plants requires that the gas be compressed to a supercritical fluid. Preliminary work [17–19] has shown that supercritical CO₂ at a pressure of 20 MPa and temperatures of 650°C causes the rapid onset of breakaway corrosion for 9 and 12Cr ferritic-martensitic steels, several austenitic stainless steels and alloys 800H, 625 and HR230.

An understanding of the carbon dioxide corrosion phenomenon requires first a review of the rather complex pattern of reaction products, followed by an analysis of the thermodynamics underlying the distribution of these products. An investigation of the mechanisms of breakaway and the transport processes which support them then allows identification of possible routes to alloy protection.

10.2 CARBON DIOXIDE CORROSION MORPHOLOGIES

10.2.1 Iron, Carbon Steels and Low Alloy Steels

Exposure of iron and carbon steel to gases rich in CO₂, but containing very little free oxygen, leads to the development of an iron oxide scale and carburisation of the underlying metal. At temperatures below 570°C, the oxide is Fe₃O₄ and develops with a duplex structure consisting of an outer layer of dense oxide and an inner porous layer [10–12,20]. Carburisation of the ferrite is evident as precipitation of Fe₃C during cooling from reaction temperature.

Low alloy steels corrode with closely similar morphologies, with chromium and molybdenum concentrating in the inner, porous scale layer. At low temperatures where wüstite is unstable, the inner layer consists of Fe₃O₄ plus the spinel, (Fe,Cr)₃O₄. At higher temperatures, the magnetite in the inner layer is replaced by wüstite. Phase constitutions of the outer layers developed in long-term reactions are summarised in Table 10.1. Carbon uptake by these steels is greater than observed in iron or carbon steel. Whereas ferrite has limited solubility for carbon, low alloy steels can precipitate chromium-rich carbides internally.

As would be expected from the high carbon diffusion coefficients (Appendix D), carburisation of chromium-bearing low alloy steels is rapid. Intergranular precipitation of (Fe,Cr)₇C₃ within a model alloy of Fe-2.25Cr penetrated the thickness of a 1.5-mm sheet within 120 h at 650°C [21]. At higher temperatures, dissolution of carbon into ferrite converts it to austenite. As a result, the subscale alloy region transforms on cooling to (ferrite + carbide) or martensite, depending on cooling rate and alloy chromium level.

As the oxide scale advances into the alloy, carbide precipitates in the subscale region are incorporated into the oxide. These carbides are oxidised, but the rate of the conversion reaction can be slow, leaving carbide residues within the inner scale layer [7,21,22].

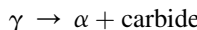
TABLE 10.1 Outer Oxide Scale Layers^a Grown on Iron-Base Alloys in Long-Term Exposure to Dry CO₂

Alloy	<i>T</i> (°C)						
	500	550	650	700	818	900	1100
Fe	M [12]						
Low alloy steels ¹	M [12,14]						
Fe-1Cr				H, M, W [7]		M [7]	W [7]
Fe-2.25Cr			H, M, W [21]		H, M, W [21]		
Fe-5Cr				H, M, W [7]		M [7]	W [7]
9–12Cr steels	H, M [22]	H, M [22,25]	H, M [22]	H [22]			
Fe-9, 10Cr			H, M, W [21,27]		H, M, W [21]	M [7]	W [7]
Fe-15Cr				H, M, W [7]		M [7]	W [7]
Fe-20Cr			E, H, M [8]	H, M, W [7]	E [21]	M [7]	W [7]
Fe-25Cr			E, H, M [8]		E [21]		
Fe-35Cr						E [23]	
441 stainless					E, MnCr ₂ O ₄ [35]		
Fe-20Cr-10Ni			H, M [8]				
Fe-20Cr-20Ni			H, M [8]		M [39]		
Ni-30Cr						E [23]	

^aPhases: E, Chromia; H, haematite; M, magnetite; W, wüstite.

10.2.2 Martensitic Chromia-Forming Steels

An important group of steels is based on compositions of Fe-(9–12)Cr-C, and examples are shown in [Table 10.2](#). When heated to temperatures in the range of approximately 910–1390°C, dilute Fe-Cr binary alloys are austenitic (Fig. 6.10). Cooling such alloys leads to their transformation back into ferrite. When carbon is also present, the phase transformations on cooling are more complex, as carbon-bearing phases such as carbides and martensite are now possible. Chromium in solution slows the reaction



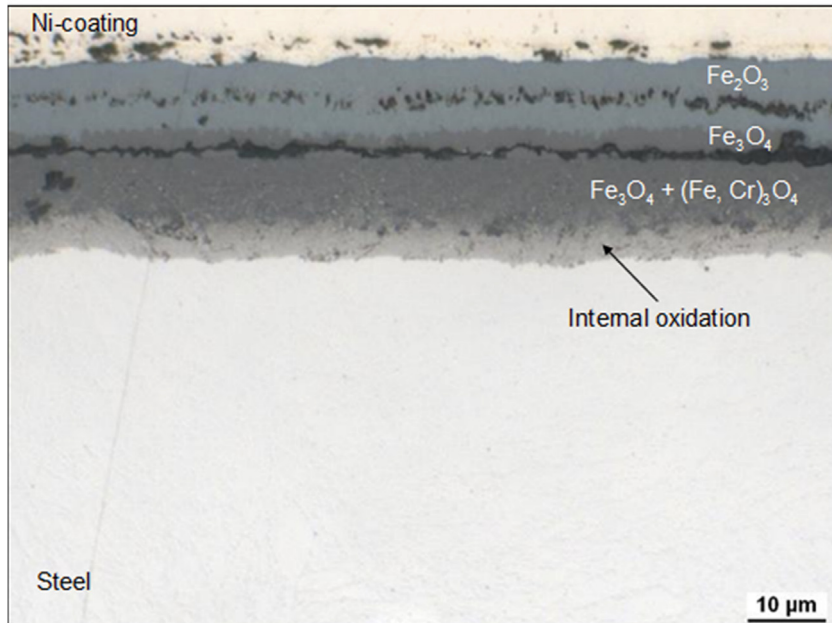
allowing austenite to be retained to lower temperatures, where the transformation to martensite can occur. The resulting microstructures, after suitable heat treatment, provide very good creep resistance at moderate temperatures. These steels are used in thermal power generation and nuclear reactors, where long-term creep rupture lives are necessary. As long-term corrosion resistance is also required, a large body of research on these materials and similar model alloys has accumulated.

Corrosion of martensitic steels by CO₂ leads to a rather rapid onset of breakaway kinetics and the growth of iron-rich oxide scales [22–28]. A typical example in [Fig. 10.3](#) shows the general features of the reaction product morphology: an outer scale region consisting of iron oxides, an inner oxide scale region containing chromium in addition to iron, an internal oxidation zone and internal carburisation. Outer-layer phase constitutions are summarised in [Table 10.1](#). Minor differences exist in reports on the makeup of the inner scale layer. Thus, the inner layer grown at 550°C on 9Cr steels has been reported to consist of Fe₃O₄ + (Fe,Cr)₃O₄ [22] or as a single-phase spinel [25]. However, agreement is general that iron-chromium spinels are a major constituent of the inner layer on these steels and on comparable Fe-Cr binary alloys. Moreover, it is clear that the inner layers usually contain more than one phase, and they are often porous. A high magnification image of the oxide-alloy interface region in [Fig. 10.4](#) shows an example of the complex inner layer microstructure [29].

TABLE 10.2 Martensitic Chromium Steel Nominal Compositions (wt%)

Common Name	Cr	C	Other
T91/P91	9	0.1	1Mo, 0.2V, 0.08Nb
T92/P92	9	0.1	2W, 0.5Mo, 0.2V, 0.05Nb
VM 12	12	0.12	2Co, 2W, 0.5Mo, 0.25V, 0.05Nb
X20	12	0.2	1Mo, 1Ni, 0.3V

(A)



(B)

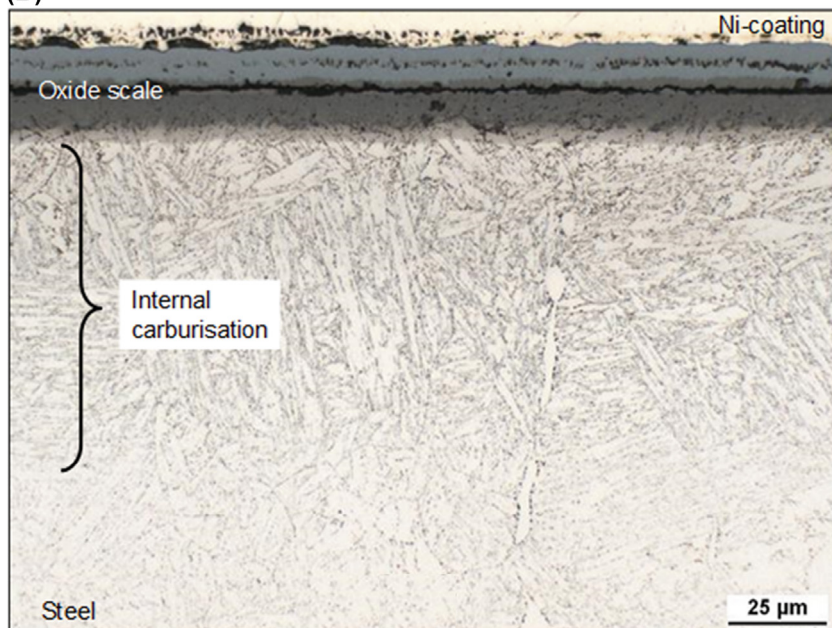


FIGURE 10.3 Cross-sections (A) unetched and (B) etched to reveal carbides of 12% Cr steel VM12 after 150 h reaction with Ar-50% CO₂ at 550°C. Reprinted from D.J. Young, P. Huczkowski, T. Olszewski, T. Hüttel, L. Singheiser, W.J. Quadakkers, *Corros. Sci.* 88 (2014) 161, with permission from Elsevier.

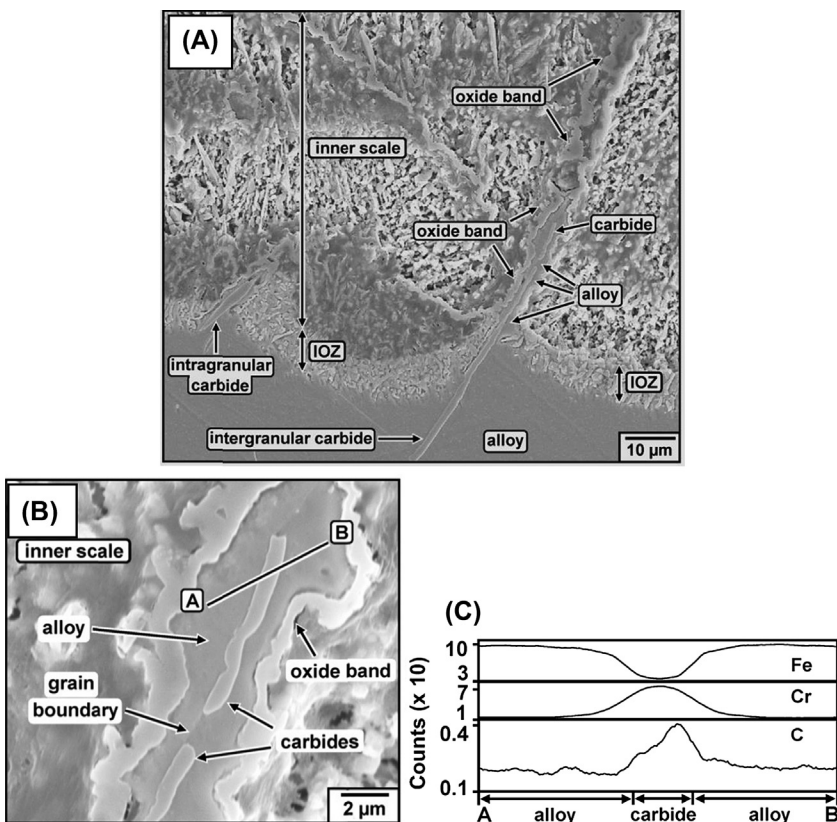


FIGURE 10.4 (A) Secondary electron SEM image of the inner scale-alloy interface of Fe-9Cr (etched with modified glyceregia solution) after reaction at 818°C in Ar-CO₂; (B) SE-SEM high magnification image of carbides in the inner scale and (C) EDX line profiles along A–B in (B). Reprinted from T.D. Nguyen, J. Zhang, D.J. Young, Corros. Sci., 89 (2014) 220, with permission from Elsevier.

Selective oxidation of chromium from martensitic steels does not occur under breakaway conditions. No depletion profiles develop within the substrate alloy, and chromium is uniformly distributed across the width of the inner scale layer [30].

Internal oxidation zones are shallow, but internal carburisation quickly extends to substantial depths [26]. Measurements by GDOES [24] of carbon concentration profiles within the steels P92 and VM12 after reaction for a number of different times with Ar-50CO₂ at 550°C established that carburisation kinetics were parabolic. An unusual feature of the carburisation reaction at this temperature is the changing boundary value of carbon concentration (or volume fraction of carbide) at the alloy-oxide interface, which increases with time, only slowly approaching a steady-state value [24,26].

The precipitates in the carburisation zones of martensitic steels have not been directly identified. However, the carbides precipitated at 650°C in binary Fe-9Cr [21] have been identified as chromium-rich $(\text{Fe},\text{Cr})_7\text{C}_3$. Just as with low alloy steels, conversion of these carbides to oxide is slow [22,31]. As seen in Fig. 10.4, they are retained within the inner scale layer, as they slowly react to form chromium-rich oxide. At higher temperatures, this conversion reaction is faster, and carbide is fully oxidised at the scale-alloy interface [7] or at an internal oxide-internal carbide interface [32].

10.2.3 Ferritic Chromia Formers

Corrosion of Fe-Cr alloys by CO_2 has been studied frequently, yielding a unified picture of the reaction morphology [7–9,21,23,33,34]. Dilute alloys exhibit breakaway corrosion, growing scales consisting of an outer layer of iron-rich oxides and an inner layer of $(\text{Fe},\text{Cr})_3\text{O}_4$, whilst carburising internally. If the chromium content of the alloy is high enough, then thin chromia scales develop. Internal carburisation is seen beneath chromia scales, but at much lower levels than beneath iron-rich oxide regions. At intermediate alloy chromium levels, a transition is observed between initially protective chromia scale growth and the development of iron-rich oxide nodules which enlarge and coalesce to form a continuous, fast growing scale (Fig. 10.5).

The level of chromium required to resist breakaway corrosion by maintaining chromia scale growth is higher than that required during exposure to oxygen [27,34]. As seen in Table 10.1, alloys containing $\leq 15\text{Cr}$ fail to passivate in CO_2 over a wide range of temperatures. Alloys with 20 or 25Cr fail at low temperatures, passivate at about 800°C and fail at higher temperatures. Meier et al. [27] compared the behaviour of a series of Fe-Cr binary alloys in CO_2 with their performance in air at 650°C. An alloy level of 10Cr

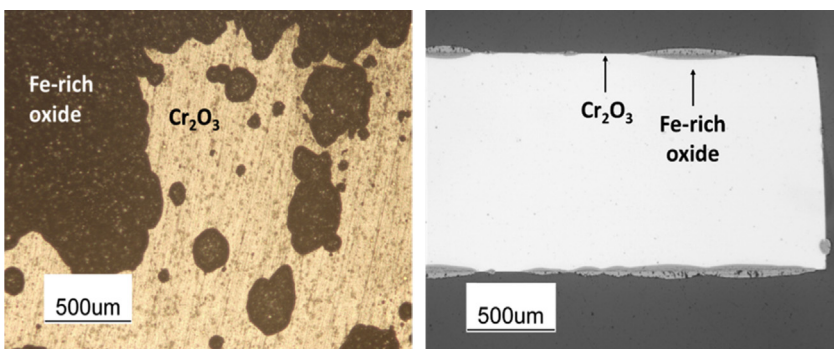


FIGURE 10.5 Plan and cross-section views showing development of iron oxide nodules on Fe-20Cr alloy exposed to $\text{Ar}-20\text{CO}_2$ at $T = 650^\circ\text{C}$. Reprinted from T. Gheno, D. Monceau, D.J. Young, *Corros. Sci.*, 64 (2012) 222, with permission from Elsevier.

was sufficient to form a Cr_2O_3 scale in air, but the critical level for chromia formation in CO_2 was between 15% and 22%.

Carburisation kinetics have been measured in some cases. Rapid parabolic kinetics for carbide precipitation beneath iron-rich oxide scales are reported [21] for Fe-9Cr at 650°C, and considerably slower rates for Fe-20Cr (Fig. 10.6). Steady-state carburisation was observed at this temperature, with a constant carbide volume fraction at the oxide-scale interface, unlike the situation reported for 9–12Cr steels at 550°C. At higher temperatures, carburisation is fast underneath nonprotective iron-rich oxide scales, forming large volume fractions of precipitate. Under chromia scales, however, much less carbide is formed, and its precipitation is commonly restricted to alloy grain boundaries. The two carbide precipitation morphologies are shown in Fig. 10.7.

Reaction of Fe-9Cr with CO_2 at 818°C leads to martensite formation in the alloy subsurface regions [21,34]. An Fe-15Cr alloy formed internal M_{23}C_6 carbides beneath an oxide scale during reaction with CO_2 at 900°C [7].

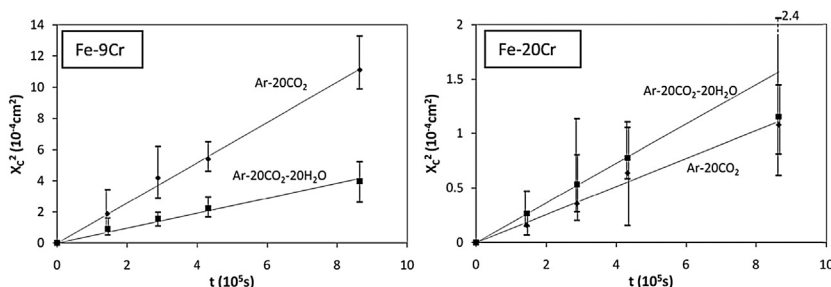


FIGURE 10.6 Internal carburisation kinetics for Fe-9Cr and Fe-20Cr reacted with Ar-20 CO_2 at 650°C. Reprinted from T. Gheno, D. Monceau, J. Zhang, D.J. Young, Corros. Sci., 53 (2011) 2767, with permission from Elsevier.

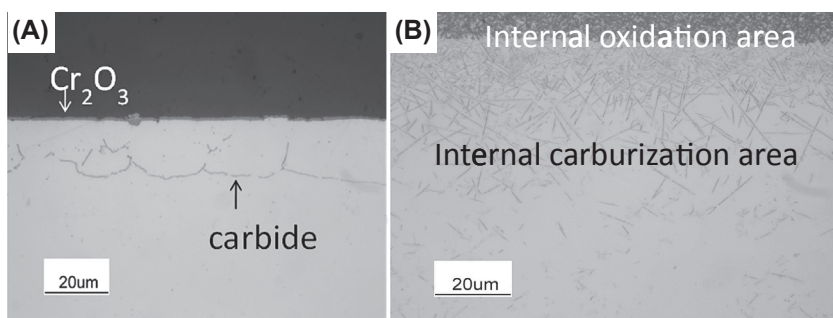


FIGURE 10.7 Internal carburisation of Fe-20Cr during reaction with Ar-20 CO_2 at 650°C: (A) under protective Cr_2O_3 scale; (B) under Fe-rich oxide scale. Reprinted from T. Gheno, D. Monceau, J. Zhang, D.J. Young, Corros. Sci., 53 (2011) 2767, with permission from Elsevier.

Reaction of 441 stainless steel (Ti, Nb stabilised 18Cr ferritic) in pure CO₂ at temperatures of 800–1000°C led to formation of a chromia scale with an outer layer of MnCr₂O₄. The underlying alloy was carburised to an undetermined extent. Chromia scaling rates were reported to be greater than those observed in oxygen [35].

10.2.4 Other Alloys

Austenitic alloys are less prone to carburisation because of their lower solubilities for carbon (see Section 9.4). Nonetheless, at sufficiently high a_C values, commercial chromia-forming austenitic alloys do carburise (Section 9.5). Reported results for various austenitic chromia formers are very consistent. Grade 304 stainless (18Cr-8Ni) develops internal oxides and carbides under an oxide scale [32,36], as does alloy 800 [32] when reacted with CO₂ at temperatures around 700°C. A Nb-stabilised 20Cr-25Ni steel reacted with CO₂ at 600–850°C is carburised internally beneath a chromia scale [37]. Similar findings have been reported [38] for this steel when reacted with CO/CO₂ gas mixtures.

Model Fe-20Ni-20Cr alloys display nonprotective behaviour in dry CO₂. At 650°C, the alloy develops a thin, protective Cr₂O₃ scale interrupted by iron-rich oxide nodules [8]. The nodules consist of an outer layer of Fe₂O₃, an intermediate layer of Fe₃O₄ and an innermost layer of FeCr₂O₄ plus NiFe₂O₄. At 818°C, an initially protective chromia scale is replaced by an Fe₃O₄ scale and an internal oxidation zone containing FeCr₂O₄ in a nickel-enriched matrix [39]. Intergranular carbides are precipitated within the alloy at 818°C, but no carburisation is observed at 650°C.

A Ni-30Cr alloy exposed to pure CO₂ at 900°C maintained a protective chromia scale and suffered no internal carburisation [23].

Very little information is available on the reaction of alumina forming alloys with CO₂. A study of the reaction between CO/CO₂ gases and several FeCrAl alloys at 1000–1200°C showed that the alumina scaling rates were the same as in air. No examination was made for internal carburisation [40].

10.2.5 Corrosion in High Pressure CO₂

Deposition of carbon has been reported to occur within the inner oxide scale layer on a number of steels and alloys. Substantial amounts of carbon were found [10] in the oxide scale grown on low alloy steels at 500°C in CO₂ containing low levels of water vapour at $p_T = 20$ atm. No such deposition was observed at a pressure of 1 atm.

Carbon deposition takes place within the inner spinel scale layer formed on 9Cr steels reacted with CO₂ at $p_T = 20$ atm and $T = 500^\circ\text{C}$ [41], and at 250 atm and 550°C [26]. Detailed examination [26] of the corrosion products of T91 steel reacted with CO₂ at 550°C revealed carbon deposited in the inner layer when $p_T = 250$ atm, but no deposit when $p_T = 1$ atm.

Short term exposures of several austenitic heat-resisting alloys (316, 253 MA and Alloy 800) to static CO₂ at 550°C and 250 atm led to the development of thin oxide scales rich in Cr, Mn, Si and Ti [42]. Little or no alloy carburisation was observed, but carbon was detected by GDOES inside the scale or at its base. Further exposure, however, leads to breakaway. Exposure of 316 to flowing CO₂ at 200 atm and temperatures of 400–600°C for periods of up to 2000 h produced a thin oxide scale over most of the surface, but iron-rich oxide nodules had started to appear, and shallow carburisation of the steel had become evident [43].

Reaction of a series of 9 and 12 Cr ferritic-martensitic steels, several austenitic stainless steels and alloys 800H, 625 and HR230 [17–19] with supercritical CO₂ at $p = 200$ atm and $T = 550$ or 650°C produces the same reaction morphologies as does corrosion by atmospheric pressure gas. However, deposition of carbon also occurs under these conditions. The location and form of the deposits have not yet been fully defined, but in the case of some autoclave tests at 200 atm and 650°C [17,19], the carbon is reported to develop on the surface of the oxide scale. For carbon to be stable in contact with the gas, sufficient CO must be present to prevent the solution loss reaction



removing the deposit. Generation of CO will always occur via the reaction of CO₂ with metal, but its actual concentration depends on the rate of total metal oxidation and the rate of fluid flow through the autoclave.

An alumina-forming austenitic stainless steel (Fe-25Ni-14Cr-3.6Al-2.5Nb-2Mn-0.5Cu) was found [44] to go into breakaway when exposed to supercritical CO₂ at temperatures of 550–650°C. Carbon was found within an internal oxidation zone beneath a complex scale which grew an outermost layer of magnetite. The substrate alloy was not examined for carburisation.

10.2.6 Summary of Findings

This brief survey of experimental findings clearly establishes that corrosion by CO₂ is much more damaging than a reaction with oxygen or air. In the case of chromia-forming alloys, the onset of rapid breakaway corrosion is accelerated. The same alloys undergo internal carburisation beneath their oxide scales. Under some conditions, elemental carbon is deposited in the scale. The questions of interest therefore concern the ways in which CO₂ can cause carbon uptake and alter the properties of otherwise protective scales.

10.3 THERMODYNAMICS AND DISTRIBUTION OF REACTION PRODUCTS

10.3.1 Oxide Scale Constitution

Carbon dioxide is oxidising to chromium and stabilises all iron oxides throughout most of the temperature range of interest (Fig. 10.8). Thus the

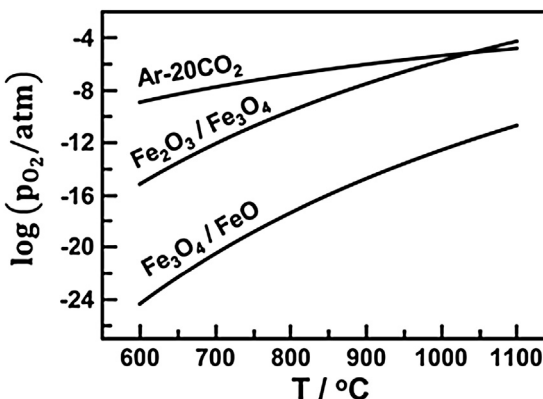


FIGURE 10.8 Equilibrium oxygen partial pressures in Ar-20CO₂ compared with stability regimes of iron oxides.

phase expected at the scale surface is either Cr₂O₃, when protection or passivation is achieved at high alloy chromium levels, or Fe₂O₃ when it is not. The sequence of phases observed in the oxide scales is as expected (Section 7.3), with the more stable chromium bearing oxides at the base of the scale and iron oxides above them. As seen in [Table 10.1](#), however, the identity of the outermost iron oxide varies with both temperature and alloy chromium level. This pattern of iron oxide formation is the result of the competition between outward flux of iron through the scale and the relatively slow surface reaction with CO₂ gas.

As the alloy chromium content increases, the volume fraction of spinel in the inner, mixed scale layer also increases. Because the spinel acts as a partial block to outward diffusion of iron, this slows the rate at which the iron reaches the surface, allowing oxygen uptake from CO₂ to convert the surface oxide to a higher oxidation state. This is seen clearly from a comparison of 9–12Cr steels with low alloy steels at 500°C. At very high alloy chromium levels, Cr₂O₃ forms rather than spinel, as expected.

Temperature also changes the nature of the outermost oxide ([Table 10.1](#)). Low alloy steels, 9–12Cr steels and dilute Fe-Cr alloys all form an outermost layer of Fe₂O₃ at temperatures of about 800°C and below. In this temperature regime, iron diffusion through the scale is relatively slow, and the CO₂ surface reaction is fast enough to enable local equilibrium at the scale-gas interface. At 900°C, however, the outer layer is Fe₃O₄, as the faster outward diffusion of iron prevents formation of haematite. At 1100°C, Fe₃O₄ is thermodynamically stable ([Fig. 10.8](#)), but wüstite is the only iron oxide formed in the time scale of the experiments, again as the result of very rapid solid-state iron diffusion.

10.3.2 Internal Carburisation

Values of the carbon activity, a_C , are usually very low in CO_2 gases. For example, in Ar-20 CO_2 at 650°C , $a_C = 1.6 \times 10^{-15}$. Nonetheless, these conditions bring about the internal precipitation of chromium-rich M_7C_3 in Fe-9Cr. The explanation was outlined qualitatively in Section 7.7, and is now treated quantitatively.

The reactions of importance are



and will be assumed to be at local equilibrium everywhere within the reacting system. As shown schematically in Fig. 7.25, the oxygen activity within the scale varies between its ambient value at the oxide/gas interface, and the dissociation pressure of the oxide at the metal/oxide interface. If carbon is present within the scale, then the $p_{\text{CO}}/p_{\text{CO}_2}$ ratio can be expressed as a function of the local p_{O_2} value through the equilibrium expression for [10.1]. At the scale-alloy interface the dissociation pressure of the oxide, $(p_{\text{O}_2})_{\text{eq}}$, yields for this ratio

$$\frac{p_{\text{CO}}}{p_{\text{CO}_2}} = \frac{K_1}{(p_{\text{O}_2})_{\text{eq}}^{1/2}} \quad [10.3]$$

where K_1 is the equilibrium constant for reaction [10.1]. This ratio depends only on the stability of the oxide, alloy composition and temperature. Then a_C is calculated from the Boudouard equilibrium [10.2] as

$$a_C = K_2 \frac{p_{\text{CO}}^2}{p_{\text{CO}_2}} \quad [10.4]$$

Although the ratio $b = p_{\text{CO}}/p_{\text{CO}_2}$ is defined by [10.3], individual partial pressures are required.

Recognising that carbon is insoluble in the oxide [45] and that CO is produced by consumption of CO_2



then the mass balance

$$p_T = p_{\text{CO}} + p_{\text{CO}_2} \quad [10.6]$$

is proposed, where p_T is an unknown value. It is then found that

$$a_C = K_2 \frac{b^2 p_T}{1 + b} \quad [10.7]$$

Thus a_C is dependent upon p_T , which is a function of both the external pressure and the scale transport properties.

The simplest assumption is that $p_T = p_{CO_2}$ (gas phase) on the proposition that CO_2 permeates the oxide scale rather freely. Gheno et al. used this approach in analysing the internal carburisation of Fe-Cr alloys in Ar-20 CO_2 [21]. At 650°C, the inner scale layer is in this case an $FeO + (Fe,Cr)_3O_4$ mixture, for which the value of $(p_{O_2})_{eq}$ is approximated [46,47] by that of $Fe_{1-\delta}O$. Proceeding on this basis, values of a_C calculated from [10.3], [10.4] and [10.7] are plotted in Fig. 10.9, superimposed on a predominance diagram for Fe-9Cr. Phase boundaries for the latter were determined from isothermal sections of the Fe-Cr-C phase diagram, generated with Thermo-Calc software [48]. Clearly, the carbon activity at local equilibrium with the oxide-alloy interface is high enough to form M_7C_3 at 650°C, thus qualitatively accounting for the observed carburisation. The quantitative success of the model is now tested by examining the amount of carbide formed.

Provided that local thermodynamic equilibrium is achieved throughout the carburisation zone, a diffusion path on the phase diagram can be used to define the compositions of coexisting phases and their mass fractions, f_m . Mass and volume fractions are related through the densities of the phases. Fig. 10.10 shows that the carbide volume fraction decreases with increasing relative depth, according to a profile which is independent of reaction time.

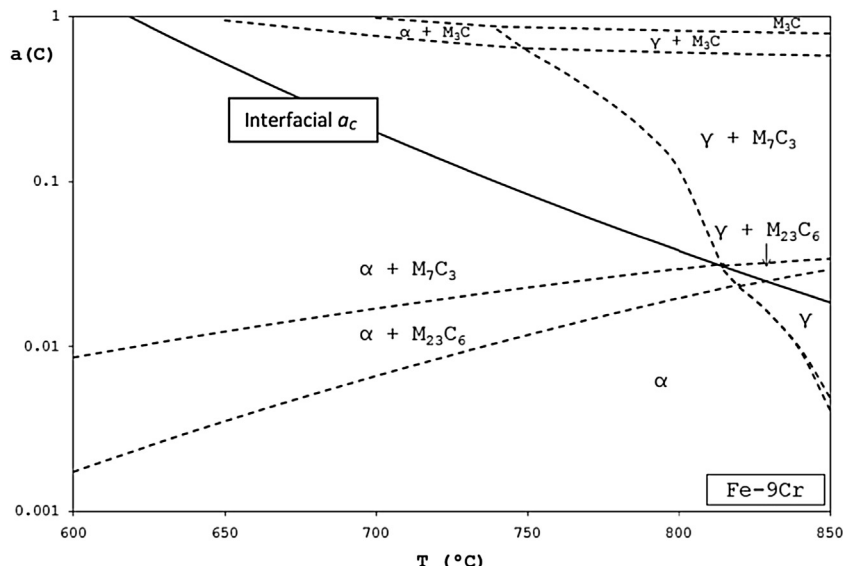


FIGURE 10.9 Interfacial carbon activity from Eq. [10.7] for p_{O_2} controlled by $Fe_{1-\delta}O/Fe$ equilibrium, and predominance diagram from data in Thermo-Calc for Fe-9Cr. Reprinted from T. Gheno, D. Monceau, J. Zhang, D.J. Young, Corros. Sci., 53 (2011) 2767, with permission from Elsevier.

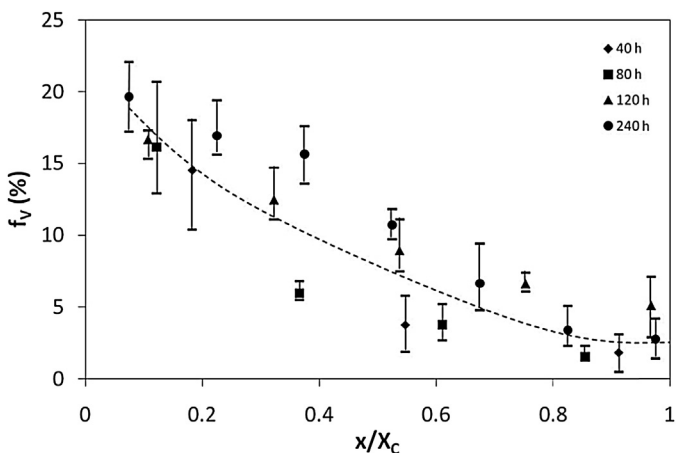


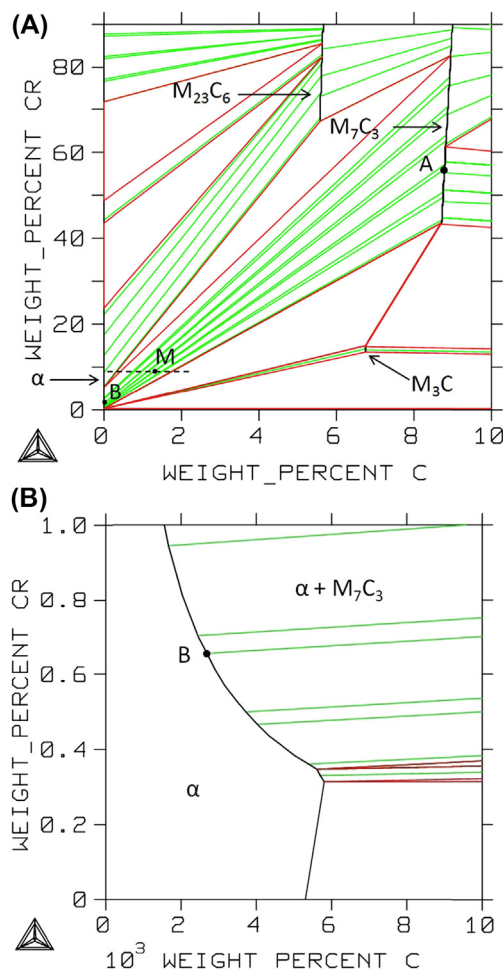
FIGURE 10.10 Carbide volume fraction in Fe-9Cr exposed to Ar-20CO₂ at 650°C plotted versus normalised position within precipitation zone after different reaction times. *Reprinted from T. Gheno, D. Monceau, J. Zhang, D.J. Young, Corros. Sci., 53 (2011) 2767, with permission from Elsevier.*

The observed steady-state distribution of phases within the precipitation zone supports the hypothesis of local thermodynamic equilibrium. To describe this, the Fe-Cr-C phase diagram shown in Fig. 10.11 was constructed using Thermo-Calc [48]. In this isothermal section, the points *M*, *A* and *B* represent the composition of the global system, the carbide precipitates and the metal matrix, respectively.

At 650°C, the diffusion coefficients D_C [21] and D_{Cr} [49] in α -Fe are estimated as 2.4×10^{-7} and $5.6 \times 10^{-14} \text{ cm}^2 \text{ s}^{-1}$, respectively. Since $D_C \gg D_{Cr}$, chromium is assumed not to diffuse on a macroscopic scale, and the diffusion path lies along the dotted line in Fig. 10.11A. This path cuts tie-lines at points corresponding to different f_m values. Expressed in terms of volume fraction, f_v , these range from 0 to 0.07 in the $\alpha + M_{23}C_6$ field and from 0.06 to 0.2 in the $\alpha + M_7C_3$ field. Experimental f_v values, shown in Fig. 10.10, thus indicate that the near interface region corresponds to M_7C_3 precipitation in ferrite, and the deeper region to $\alpha + M_{23}C_6$. Analysis by XRD of the subsurface alloy zone in reacted Fe-9Cr confirmed the identity of the carbide as M_7C_3 .

Using the lever rule, a tie-line in the $\alpha + M_7C_3$ field corresponding to the volume fraction measured at the interface between internal oxidation and carburisation zones is selected. This defines (Fig. 10.11B) the carbon content of the metal matrix, $N_C^{(i)}$. Thermodynamic data obtained from Thermo-Calc for the dissolution of carbon in α -(Fe,Cr) then lead to the local equilibrium carbon activity. The amount of carbide formed during reaction with Ar-20CO₂ is found in this way to correspond to $\alpha_C = 0.43$. This is to be compared with the

FIGURE 10.11 Isothermal section of the Fe-Cr-C phase diagram at 650°C calculated from ThermoCalc: (A) overall view; (B) Fe-rich corner.



value of 0.52 calculated from scale-alloy equilibrium (Eq. [10.7]). This good agreement demonstrates the applicability of the local equilibrium description.

Further confirmation is available from the carburisation rates. The observed parabolic kinetics (Fig. 10.6) indicate diffusion control, and the rate constant k_p is related to carbon permeability (Section 9.4.2). According to Wagner's approximate equation [50]

$$X_C^2 = 2k_p t \quad k_p = \frac{N_C^{(s)} D_C}{v N_{\text{Cr}}^{(0)}} \quad [10.8]$$

where $N_C^{(s)}$ is the surface concentration of carbon in the metal matrix, v the C/Cr ratio in the carbides and $N_{\text{Cr}}^{(0)}$ the initial Cr mole fraction in the alloy.

Diffusional blocking by the small precipitates is ignored. In the presence of an external oxide scale, the surface concentration of carbon, $N_C^{(s)}$, is replaced by the interfacial value, $N_C^{(i)}$. A value of $k_p = 6.5 \times 10^{-10} \text{ cm}^2 \text{ s}^{-1}$ is found from Fig. 10.6 for Fe-9Cr reacted in Ar-20CO₂. Use of this along with the value [51] $D_C = 2.4 \times 10^{-7} \text{ cm}^2 \text{ s}^{-1}$ and $\nu = 0.345$ (an average for Cr₂₃C₆ and Cr₇C₃) in (9) leads to the estimate $N_C^{(i)} = 9.2 \times 10^{-5}$, which corresponds very closely to the value $a_C = 0.43$ estimated from the phase diagram and carbide volume fraction.

However, for Eq. [10.9] to hold, (1) the condition $N_C^{(i)} D_C \ll N_{\text{Cr}}^{(0)} D_{\text{Cr}}$ must be met, (2) carbon must react with chromium but not iron and (3) the carbides must be sufficiently stable for both chromium and carbon concentrations in the metal matrix to be negligible throughout the precipitation zone. Although the permeability condition is satisfied, the other two conditions are not. As is clear from the phase diagram in Fig. 10.11, the carbides dissolve substantial amounts of iron. Furthermore, precipitation of chromium is incomplete, and the extent varies across the precipitation zone (Fig. 10.10), reflecting the local equilibrium requirement for higher matrix N_{Cr} values to stabilise the precipitates at the lower a_C values prevailing in the inner parts of the carburisation zone. These complexities have been dealt with by numerical calculation [21] based on the partial precipitation description provided by Ohriner and Morrall [52] (see Section 6.6). The more accurate treatment of carburisation kinetics yields a value of $a_C = 0.25$, still in reasonable agreement with the predictions of local thermodynamic equilibrium.

Carbon activity values have been calculated in the same way from experimental results obtained for Fe-20Cr reacted at 650°C in Ar-20CO₂ and are summarised in Table 10.3, along with results for Fe-9Cr. As reflected in the slower carburisation rates and smaller precipitate volume fractions observed for Fe-20Cr, the oxide-alloy interfacial carbon activity is much lower than for Fe-9Cr. As the oxide scales were different — iron-rich oxides on Fe-9Cr and chromia interrupted by iron oxide nodules on Fe-20Cr — it seems likely that the carbon permeability of these scales was also different. The discussion returns to this point in Section 10.5.

TABLE 10.3 Carbon Activity at the Scale/Alloy Interface for Fe-9Cr and Fe-20Cr Alloys Reacted at 650°C [21]

Alloy	Gas	Experimental		Thermodynamic Equilibrium
		From k_p	From f_v	
Fe-9Cr	Ar-20CO ₂	0.25	0.43	0.52
	Ar-20CO ₂ -20H ₂ O	0.07	0.21	
Fe-20Cr	Both	0.01	0.1	

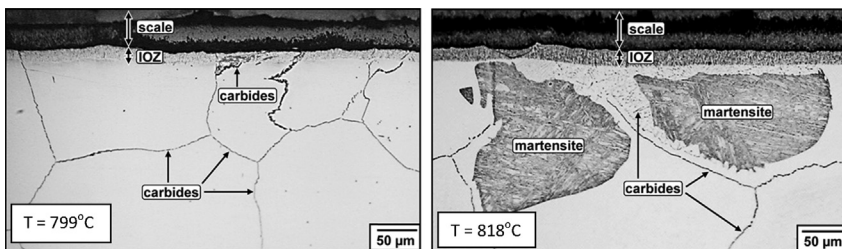
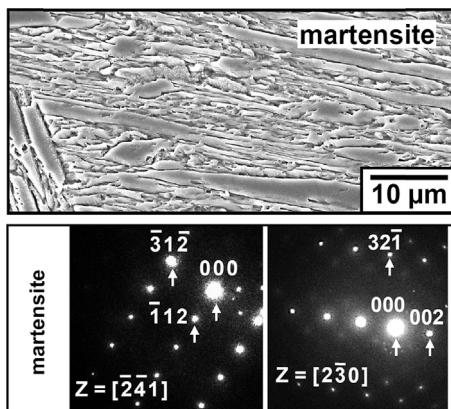


FIGURE 10.12 Cross-sections of Fe-9Cr after reaction for 20 h in Ar-20CO₂ at 799 and 818°C. Reprinted from T.D. Nguyen, J. Zhang, D.J. Young, *Scripta Mater.* 69 (2013) 9, with permission from Elsevier.

A different form of carburisation is observed in Fe-9Cr at higher temperatures [34]. As seen in Fig. 10.12, reaction in CO₂ leads to the formation of martensite, as well as carbides at 818°C, but not at 799°C where only carbides result. Identification of the martensite by TEM is illustrated in Fig. 10.13. The selected area electron diffraction (SAED) patterns match well with the body-centred tetragonal lattice of martensite, with $a = 0.292$ nm and $c/a = 1.06$. Microhardness measurements of HV (martensite) = 461 and HV (ferrite) = 114 confirm the transformation. These observations can be understood from the Fe-Cr-C phase diagram.

The maximum carbon activity calculated from Eqs [10.1] and [10.2], using a value of p_{O_2} set by equilibrium at the oxide scale-alloy interface [21] at 799 and 818°C is about 0.03. This is seen from Fig. 10.9 to be higher than the equilibrium values required to form austenite at 818°C, but not at 799°C where the phase is not accessible. Isothermal sections calculated from Thermo-Calc in Fig. 10.14 show this more clearly. The diffusion paths mapped onto these diagrams correspond to $D_C \gg D_{Cr}$, and show how austenite is formed only at the higher temperature.

FIGURE 10.13 High magnification SEM image of martensite from Fig. 10.12, and SAED patterns showing its tetragonal symmetry. Reprinted from T.D. Nguyen, J. Zhang, D.J. Young, *Scripta Mater.* 69 (2013) 9, with permission from Elsevier.



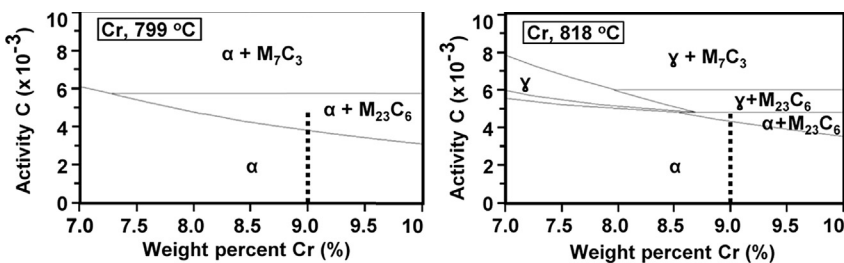


FIGURE 10.14 Isothermal sections of Fe-Cr-C phase diagram calculated from ThermoCalc, with schematic diffusion paths for rapid inward diffusion of carbon.

The CCT diagram of P91 steel [53], which has a similar Cr content (Table 10.2), is shown in Fig. 10.15. Cooling curves measured [34] after a reaction of Fe-9Cr at 799 and 818°C and superimposed on this diagram are far from the nose of the austenite to ferrite transformation curve, showing that the cooling rate was fast enough to transform austenite to martensite, explaining the formation of the latter after austenite had been formed by carburisation.

10.3.3 Carbon Deposition

As seen above, the maximum values of a_C beneath iron oxide scales were calculated to be 0.52 at 650°C and 0.03 at 818°C, showing that deposition of elemental carbon is impossible at these temperatures and the assumed value of $p_T = 0.2$ atm. Deposition of carbon at lower temperatures is readily understood from the thermodynamics of the exothermic Boudouard reaction (Section 9.2).

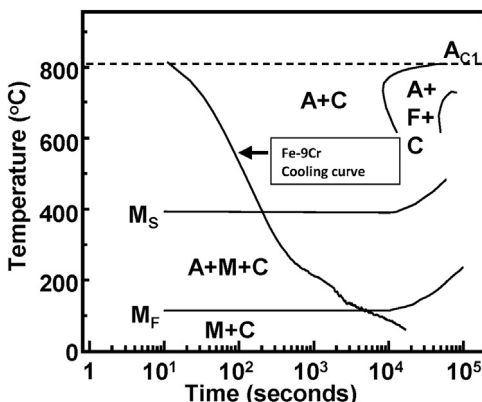
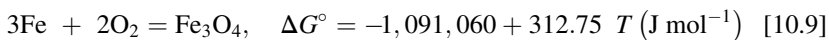


FIGURE 10.15 Continuous cooling transformation curve for P91 [52], showing measured cooling trace for the Fe-9Cr specimen in Fig. 10.12. Reprinted from T.D. Nguyen, J. Zhang, D.J. Young, *Scripta Mater.* 69 (2013) 9, with permission from Elsevier.

At temperatures below 570°C, wüstite does not exist, and the scale-gas equilibrium oxygen pressure, $(p_{O_2})_{eq}$, is calculated from



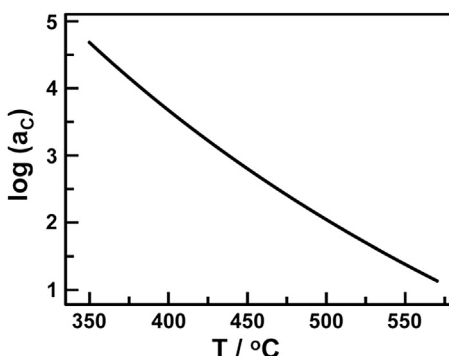
If $(p_{CO} + p_{CO_2}) = 1 \text{ atm}$, then Eq. [10.7] yields the a_C values shown in Fig. 10.16. For example, at 500°C, $(p_{O_2})_{eq} = 2.0 \times 10^{-29} \text{ atm}$, $a_C = 65$, and deposition of elemental carbon within the inner oxide layer is predicted on this basis. Experimental investigation [10] showed, however, that none occurred at $p_T = 1 \text{ atm}$, although large amounts were deposited at $p_T = 20 \text{ atm}$ [10,41]. As seen in Eq. [10.7], for a given value of $(p_{O_2})_{eq}$ (and therefore of b), a_C increases in proportion to p_T . The precipitation of carbon during a reaction with high-pressure (including supercritical) CO₂ is accounted for on this basis. The driving force for carbon deposition becomes even greater at lower temperatures, but the kinetics of the deposition reaction are also much slower.

It is apparent that the precipitation of carbon requires a high degree of gas phase supersaturation. As a homogeneous gas phase process, the Boudouard reaction is very slow, reflecting the difficulty of nucleating graphite. The presence of water vapour aids the carbon deposition reaction in oxide scales grown in CO₂ [10], presumably because the synthesis gas reaction [9.7] is faster than the Boudouard one.

Carbon activities at the oxide scale-alloy interface are far greater than in the gas, and in the case of iron-rich scales, can approach local equilibrium with the low oxygen potential through the Boudouard reaction. When steady-state conditions are achieved, the pattern of alloy carburisation beneath oxide scales during reaction with CO₂ has been demonstrated to be in accord with local equilibrium, as described by Fe-Cr-C phase diagrams, and the high carbon activities predicted from local equilibrium. Carbon deposition within the oxide scale at high p_{CO_2} is also qualitatively in accord with the predictions of local thermodynamics.

If carbon can approach thermodynamic equilibrium within and beneath the oxide scale, this raises the obvious questions as to how carbon enters and

FIGURE 10.16 Carbon activity beneath Fe₃O₄ scales calculated from Boudouard equilibrium with $[p(\text{CO}_2) + p(\text{CO})] = 1 \text{ atm}$.



penetrates the scale, and what effect it might have on the protective character of that scale. The latter question is considered first, by examining the breakaway phenomenon.

10.4 MECHANISM OF BREAKAWAY

Questions of interest concern the way in which rapid iron oxide growth initiates, the mass transport mechanisms which sustain the fast growth, the related question of why the alloys do not repassivate and how carbon deposition can occur. The transition from protective, chromium-rich scale growth to fast-growing iron-rich oxides is so fast in the case of alloys containing less than about 15% Cr that the initiation process has not been studied. The initiation step on higher chromium alloys has been examined and provides insight into the general nucleation process.

10.4.1 Iron Oxide Nodule Nucleation

As seen in [Figs 10.1 and 10.5](#), iron-rich oxide nucleates as nodules at seemingly random locations on chromia-covered alloy surfaces. The nodule in [Fig. 10.1](#) is at an advanced stage of its evolution and has achieved the phase distribution characteristic of long-term breakaway scaling. An understanding of its original genesis requires examination of the early stages of nodule formation.

Such a nodule formed on Fe-20Cr at 650°C is shown in [Fig. 10.17](#), together with an EDAX profile measured along the right-hand arrow. The nodule is seen to consist of iron-rich oxide growing over a thin, chromium-rich oxide layer which is continuous with the surrounding protective oxide. An internal oxide containing comparable concentrations of iron and chromium lies beneath the centre of the nodule, and a thin band of chromium-rich carbide has formed parallel to the alloy surface. Because the EDAX measurements are qualitative in the nonmetallic phases, they cannot be used for phase identification. Raman spectra shown in [Fig. 10.17C](#) are used with reference data [54] to identify the protective scale (zone 1) as Cr-rich M_2O_3 , the nodule outer layer (zone 2) Fe-rich M_2O_3 , the layer which is continuous with the protective scale (zone 3) as Cr-rich M_2O_3 and the internal oxide particles (zone 4) as $Fe_{1.4}Cr_{1.6}O_4$ spinel.

Because chromia is more stable than $FeCr_2O_4$, the finding of internal chromium-rich spinel beneath a Cr_2O_3 layer (region 3 in [Fig. 10.17](#)) is inconsistent with steady-state local equilibrium with an oxygen activity which decreases from the scale into the alloy. This reflects the transient nature of the nodule, which has yet to evolve its steady-state morphology. Examination of chromium depletion profiles within the alloy provides insight into this process.

Two cross-sections from the same specimen of Fe-20Cr reacted with Ar-20CO₂ at 650°C are shown in [Fig. 10.18](#), with internal carbides present in

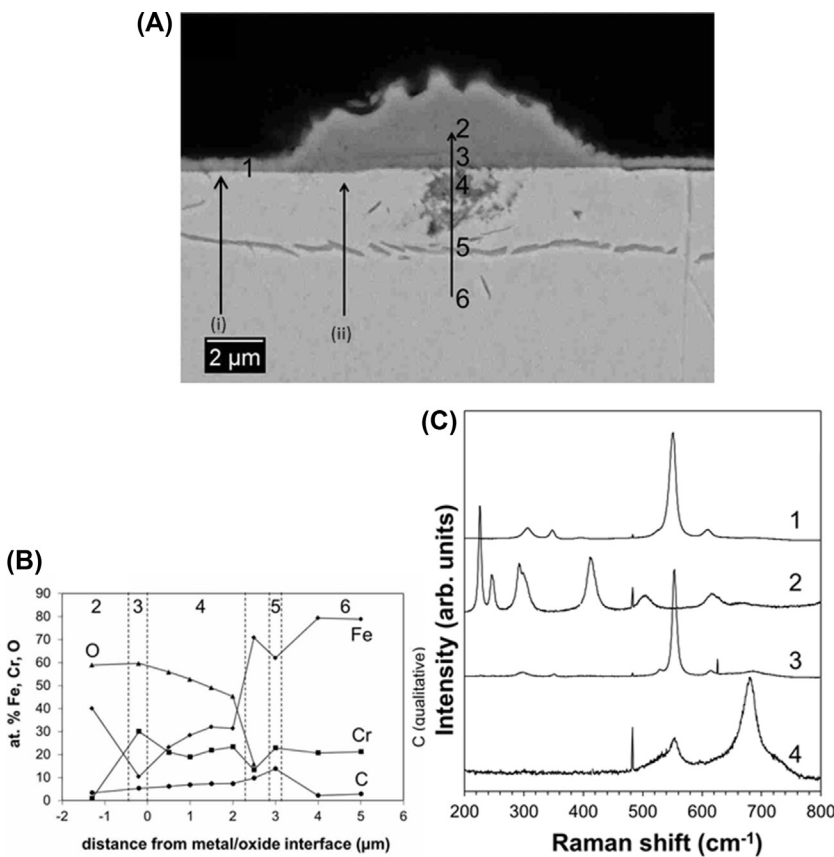


FIGURE 10.17 Early stage nodule on Fe-20Cr exposed to Ar-20CO₂ at 650°C: (A) cross-section, (B) EDAX profile showing compositions at points marked on (A) and (C) Raman spectra of oxide phases at positions marked in cross-section. *Reprinted from T. Gheno, D. Monceau, D.J. Young, Corros. Sci., 64 (2012) 222; T. Gheno, D. Monceau, D.J. Young, Corros. Sci., 77 (2013) 246, with permission from Elsevier.*

one case but not the other. Chromium depletion profiles were measured in numerous locations and are grouped together in Fig. 10.18B and D according to local scale thickness, $X_{\text{Cr}_2\text{O}_3}$, which varied considerably over the specimen surface [8]. Wagner's diffusion analysis (Section 5.4) is now used to evaluate these profiles.

Chromium depletion was limited to about 5 μm, whereas the specimens were more than 1 mm thick. Clearly, at the low experimental temperature, Cr₂O₃ growth is too slow for the depletion profiles generated on the opposed faces of a specimen to overlap in the time frame considered. Alloy-scale interfacial chromium mole fractions, N_{Cr}^i , were calculated on the

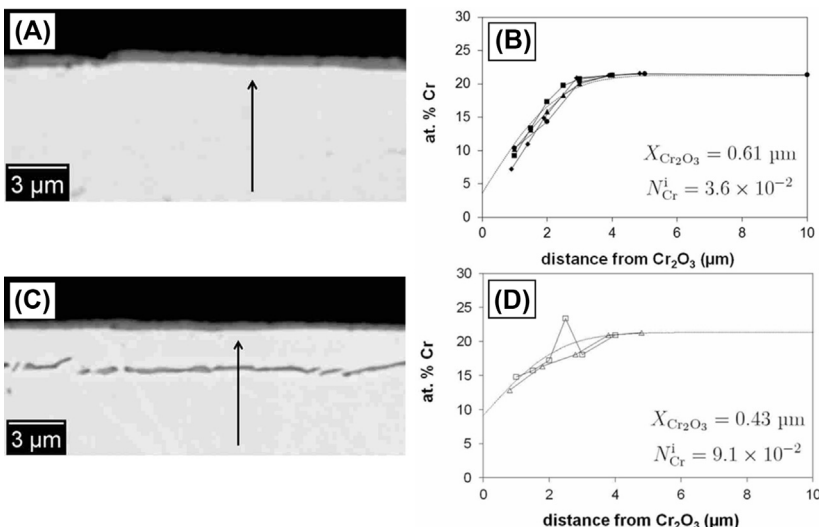


FIGURE 10.18 Cross-sections from the same specimen of Fe-20Cr reacted with Ar-20CO₂ at 650°C for 80 h: (A) no internal carbide and (B) corresponding subsurface EDAX profiles; (C) with internal carbide and (D) corresponding EDAX profile shown by symbols □, compared with carbide-free zone (Δ). Reprinted from T. Gheno, D. Monceau, D.J. Young, Corros. Sci., 77 (2013) 246, with permission from Elsevier.

assumption that the scale is pure Cr₂O₃, using the steady-state equation given by Wagner [55]

$$\frac{N_{\text{Cr}}^0 - N_{\text{Cr}}^i}{1 - N_{\text{Cr}}^i} = F \left[\frac{2V_{\text{alloy}}}{V_{\text{Cr}_2\text{O}_3}} \sqrt{\frac{k_{\text{p},\text{Cr}_2\text{O}_3}}{2D_{\text{Cr}}}} \right] \quad [10.10]$$

where F is a function defined in [5.26] and the rate constant $k_{\text{p},\text{Cr}_2\text{O}_3}$ is defined by

$$X_{\text{Cr}_2\text{O}_3}^2 = 2k_{\text{p},\text{Cr}_2\text{O}_3}t \quad [10.11]$$

Molar volumes and diffusion coefficient are assumed not to vary with alloy composition.

Because the severity of depletion varied with the local oxide thickness, $k_{\text{p},\text{Cr}_2\text{O}_3}$ values were estimated for each location using the measured oxide thickness and reaction time. Values of N_{Cr}^i deduced from Eq. [10.3] are then used to calculate depletion profiles using the appropriate solution of Fick's second law of diffusion for a semi-infinite solid [56]

$$\frac{N_{\text{Cr}}(x, t) - N_{\text{Cr}}^i}{N_{\text{Cr}}^0 - N_{\text{Cr}}^i} = \operatorname{erf} \left(\frac{x}{2\sqrt{D_{\text{Cr}}t}} \right) \quad [10.12]$$

where x is the distance from the metal/oxide interface. The calculated profiles are shown as dotted lines in Figs 10.18 and 10.19.

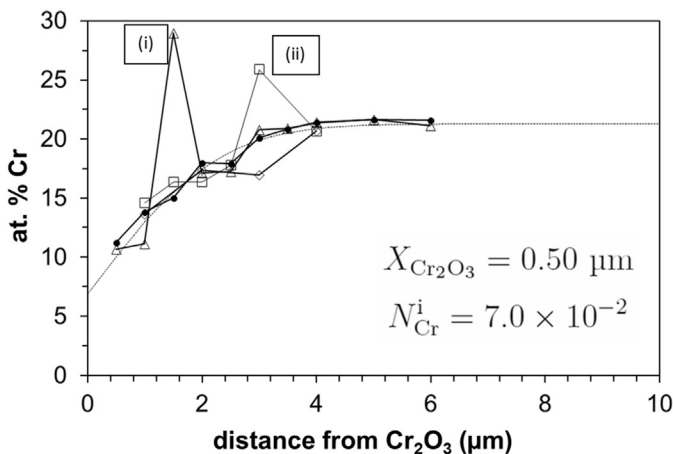


FIGURE 10.19 Chromium depletion profiles: (i) beneath protective scale and (ii) beneath nodule, at locations shown in Fig. 10.17A.

Chromium depletion profiles recorded in carbide-free zones (filled symbols in Fig. 10.18B and open triangles in Fig. 10.18D) are seen to match the calculated profiles very well, and significant changes in N_{Cr}^i accompany local variations in scale thickness on the same specimen. The success of Eq. [10.10] in relating chromium depletion to chromia scaling rate, despite local variations in the two quantities, shows that the mass balance underlying the equation is correct. In other words, the composition of the protective scale does not change significantly, and variations in its growth rate have some other cause. As diffusion in chromia scales at this temperature is predominantly via grain boundaries, it seems likely that local variations in oxide grain size and/or shape are responsible.

The observed variations in $X_{\text{Cr}_2\text{O}_3}$ and N_{Cr}^i along the scale interface are large. Although the steady-state analysis of (10.10)–(10.12) succeeds when applied locally, the alloy-scale system as a whole is characterised by a boundary condition which varies with lateral position. Thus the system is not in a uniform steady state. Rather, it should be thought of as subject to fluctuations which are not quickly removed. The process for their removal – lateral diffusion of alloy chromium parallel to the scale interface – is slow compared to chromium diffusion toward the scale, because the concentration gradients involved are smaller.

The question now is whether the observed fluctuations in scaling rate and alloy depletion can destabilise the protective chromia layer. Chemical failure occurs when the interfacial value of a_{Cr} becomes low enough for spinel formation via Eq. [2.91]. Calculation of this value using the method of Section 2.4.2 yields a minimum value, $N_{\text{Cr}}^* = 1.2 \times 10^{-5}$ at 650°C . Kinetic stability of

chromia growth, according to Eq. [10.10], is achieved if $N_{\text{Cr}}^i \geq 0$, so the requirements are essentially the same.

If a protective chromia scale is present, as is required for a depletion measurement, then by definition the condition is met. Evaluation of N_{Cr}^i is nonetheless useful, as it provides a guide as to how close an alloy might be to breakaway. In the case of Fe-20Cr reacted in dry CO_2 at 650°C , Eq. [10.10] yields $N_{\text{Cr}}^i = (6.9 \pm 4.6) \times 10^{-2}$, measured [8] after 40–240 h of reaction. Thus the surplus of chromium is variable and sometimes small. If fluctuations in the scaling rate are greater, then they could lead to its kinetic instability. In addition, scale cracking or spallation can expose the depleted alloy to the reacting gas. Reformation of chromia at the relatively fast rate typical of initial growth causes an increase in the outward chromium flux, and N_{Cr}^i first decreases before returning to the steady-state value [57]. If N_{Cr}^i falls below N_{Cr}^* during this transient stage, chemical failure occurs.

Local chromium depletion is unaffected by carbide precipitation. The concentration profiles shown in Fig. 10.18D correspond to two locations where the chromia scale had the same thickness. Despite the precipitation of chromium-rich carbide in one of these, the overall profile is the same as that in a carbide-free location, apart from local enrichment in the precipitate. The limited carbide precipitation occurring in Fe-20Cr beneath a protective Cr_2O_3 scale does not change the interfacial chromium concentration, the value of which is critical to the resistance of the alloy to breakaway. Thus N_{Cr}^i values were similar and related in the same way to $X_{\text{Cr}_2\text{O}_3}$, independently of whether or not carbide precipitated. Indeed, the initial formation of nodules was independent of the presence or absence of internal carbide beneath the chromia scale.

Beneath the early stage nodule in Fig. 10.17 lies a Cr-rich oxide layer which appears to be continuous with the surrounding, protective Cr_2O_3 scale. In fact, this layer evidences quite different behaviour at the nodule centre, where internal oxidation has commenced, and its periphery. The depletion profile recorded below the outer part of the small nodule, marked as (ii) in Fig. 10.17A, is shown in Fig. 10.19. No significant difference is seen between it and other profiles recorded underneath the protective Cr_2O_3 scale, away from any Fe-rich nodule. Thus, the depletion in chromium concentration is unchanged, despite the fact that the outer layer located directly above is pure iron oxide (Fe_2O_3). This apparent contradiction with local mass balance shows that outward iron diffusion across the metal/oxide interface to form Fe_2O_3 did not occur at position (ii), but elsewhere, in the centre of the nodule, at a location where the chromia layer had lost its protective character. This was the site of nodule initiation. Lateral iron diffusion allowed spreading of the Fe_2O_3 nodule above the still protective chromia layer at position (ii) in Fig. 10.17A.

10.4.2 Mass Transport Processes

The mechanism of breakaway oxidation may be described as follows: initially, the alloy surface is covered by a protective Cr_2O_3 scale, which generates a subsurface chromium-depleted zone. Failure of the Cr_2O_3 scale occurs locally, either mechanically or by fluctuations in $k_{\text{p},\text{Cr}_2\text{O}_3}$ leading to chemical failure. The chromium-depleted alloy is exposed to the atmosphere and, unable to reform Cr_2O_3 , produces spinel. Töpfer et al. [58] showed that the iron tracer diffusion coefficient is about three orders of magnitude higher than that of chromium over a range of oxygen activity in $\text{Fe}_{3-x}\text{Cr}_x\text{O}_4$ spinels, with $0 < x < 0.4$, at 1200°C. This observation is likely to hold, at least qualitatively, at lower temperatures. Thus, the outward cation flux across the newly formed spinel oxide consists mainly of iron, and an outer Fe_2O_3 layer forms. In addition, a higher interfacial oxygen activity accompanies spinel formation, and oxygen permeability rises until outward chromium diffusion from the depleted alloy is insufficient to prevent internal precipitation of Cr-rich spinel.

At first, the fluxes of iron and oxygen are localised in the centre of the nodule, and the nearby alloy is not affected. A subscale alloy matrix at local equilibrium with the internal spinel precipitate results, and the interfacial chromium activity is too low to stabilise Cr_2O_3 . As oxygen diffusion into the alloy is lateral as well as inward, internal precipitation and conversion of the Cr_2O_3 layer to spinel oxide both spread laterally. Since fast iron and oxygen diffusion across the originally protective layer is limited to a central region, whereas the inner and outer parts may grow in all directions, the nodule assumes an elliptical shape. Then, as oxygen diffuses inward, the depth of the internal oxidation front increases, while the metal matrix surrounding the internal Cr-rich spinel particles is subsequently oxidised into an Fe-rich spinel. The observed two-phase, inner oxide layer results. Fast outward iron diffusion results in the formation of Fe_3O_4 beneath the first formed Fe_2O_3 . Further lateral growth of the nodules leads to their coalescence to form a more or less uniform scale.

As noted above, the inner scale layer is porous, and gas phase transport within this layer is therefore possible [14,26]. For this to be important, significant partial pressures must be available, a question discussed in Sections 2.9, 10.5 and 11.4. Growth of the outer iron oxide layers is supported by continuing outward diffusion of iron through the iron-rich component of the scale inner layer.

Very high volume fractions of internal oxides form beneath this scale. In the case of Fe-20Cr discussed above, $f_{\text{v-ox}} = 0.7 \pm 0.1$, a level far exceeding the value of 0.3 generally thought [59] to be sufficient for the transition from internal to external oxidation. The oxides form such a dense precipitation zone rather than a continuous layer because they are produced by *in situ* oxidation of pre-existing internal carbides [7,22].

Extensive carburisation beneath the Fe-rich oxide nodules and scales causes massive chromium depletion in the alloy matrix, and carbide dissolution cannot sustain the chromium flux required to reform a Cr-rich layer at the base of the scale [2]. Thus whilst internal carburisation is a consequence, not a cause, of the onset of breakaway, subsequent oxidation of the carbides permanently immobilises the chromium, making scale rehealing impossible. Iron-rich oxide formation, together with in situ oxidation of chromium (in the form of internal carbides, internal oxides and Cr-rich oxide particles in the inner scale), are thus continued in a rapid but steady-state reaction.

10.4.3 Carbon Deposition and Breakaway Corrosion at High Pressures

Although steels and alloys containing less than about 15% Cr form fast-growing, iron-rich scales very early when attacked by CO₂, a subsequent, even faster breakaway reaction ensues if carbon deposits form within the scale. As seen above, low temperatures and high pressures lead to much higher carbon activities within oxide scales, and carbon deposits are therefore expected on thermodynamic grounds.

Carbon deposition is thought to degrade the protective character of the inner layer by volume expansion leading to scale fracture [10], by preventing oxide sintering and preserving a microporous structure [11] or by increasing the porosity [26].

There remain two unanswered questions: how does carbon penetrate the oxide scale, and what causes the fluctuations in chromia scaling rates? As is now discussed, the two phenomena may well be related.

10.5 CARBON PENETRATION OF OXIDE SCALES

The solubility of carbon in FeO, Fe₃O₄ and Cr₂O₃ has been found to be immeasurably small [45], and understanding the mechanism whereby carbon passes through scales of these oxides necessitates consideration of their microstructure. It is clear that chromia provides a much more successful, albeit imperfect, barrier to carbon entry than do iron-rich oxide scales (see Fig. 10.7). Possible carbon transport mechanisms in the latter have been studied for some time, and are considered first.

10.5.1 Carbon Penetration of Iron-Rich Oxide Scales

Breakaway scales grown by ferrous alloys in CO₂ consist of an outer layer of essentially pure iron oxides (Table 10.1) and an inner layer containing chromium (and molybdenum if present) as well as iron. The inner layer is sometimes described as porous [10–12,20,25,26], and an example of this morphology is shown in Fig. 10.4. In other cases, however, any porosity within

the inner layer is widely dispersed ([Fig. 10.3](#)). Although inner layer microstructures may vary, outer layers appear always to be dense and compact.

Long ago, Fujii and Meussner summarised in their much cited paper [[7](#)] the conceptual difficulties in understanding carbon penetration. Either carbon diffuses rather readily through the oxide or it passes as gaseous CO_2 through open pore space. In the latter case, however, gaseous diffusion would be rapid, leading to oxygen and carbon activities beneath the scale similar to those of the surrounding environment. These conditions would be decarburising to the alloy, and at variance with the experimental results. As has since been shown [[45](#)], carbon cannot dissolve in iron oxides, and its entry into the scale via solid-state diffusion is also impossible.

A solution proposed for this problem is diffusion of CO_2 molecules through the almost completely dense outer oxide via microchannels [[11](#)] or nanopores [[26](#)]. Depending on the dimensions of these channels, and their frequency of occurrence, a value for D_{CO_2} consistent with both the rate of inner layer growth and the requisite low p_{O_2} value at the pore base could be arrived at. At the moment, no evidence is available for the existence of such pores.

A further difficulty with this model is that the pore inner walls exposed to gaseous CO_2 would grow more iron oxide, filling the pore and blocking further access by gas species. It is possible, of course, that a continuing process of pore blockage accompanied by new pore formation could provide ongoing gas access to the inner part of the scale. Again, experimental evidence for any such process is lacking.

Despite the failure so far to identify CO_2 pathways through the outer, dense oxide scale, it is clear that both carbon and oxygen do transfer across this barrier, forming both new oxide in the inner scale layer, and carbide precipitates within the alloy. Inward oxygen transfer was confirmed by isotope experiments involving two-stage reaction in C^{18}O_2 and C^{16}O_2 , which led to the detection of the second stage oxidant in the inner scale layer [[33](#)]. The continuation of carbon transport as the outer oxide layer thickens is clear from the steadily increasing penetration of carbon into the alloy.

Examples of steady-state, parabolic carburisation kinetics observed at 650°C are shown in [Fig. 10.6](#). Evidently the rate of carbon permeation of the oxide is sufficient to maintain an essentially constant a_{C} value at the scale-alloy interface. This is not the case at lower temperatures, where the carbon level at this interface increases with time [[24,25](#)]. This situation of nonsteady-state carburisation is examined further in order to better characterise the carbon transmission mechanism.

10.5.2 Nonsteady-State Carburisation Under Iron Oxide Scales

Carbon concentration profiles developed within a P91 steel reacted with Ar- 50CO_2 at 550°C are shown in [Fig. 10.20A](#). The maximum concentrations are located at the oxide-alloy interfaces, and the time evolution of these values is

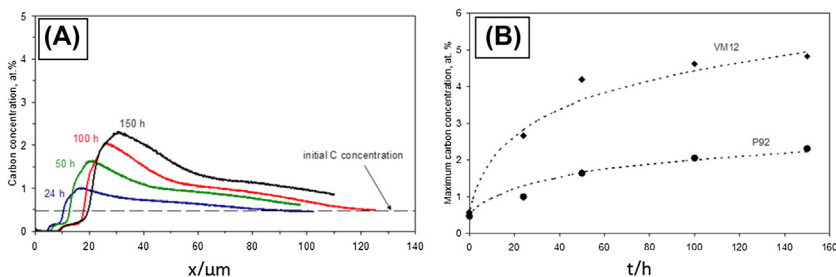


FIGURE 10.20 (A) Carbon concentration profiles (measured by GDOES) in 9% Cr steel P92 after different times of reaction in Ar-50% CO₂ at 550°C. (B) Carbon concentration at oxide-alloy interface in P92 and VM12. *Reprinted from D.J. Young, P. Huczkowski, T. Olszewski, T. Hüttel, L. Singheiser, W.J. Quadakkers, Corros. Sci., 88 (2014) 161, with permission from Elsevier.*

shown for two steels in Fig. 10.20B. As the solubility of carbon in ferrite is low (Fig. 10.11 shows values for 650°C), the measured concentration approximates very closely to the amount present in carbide precipitates. Increasing carbide volume fractions near the scale/alloy interface therefore reflect continued precipitation, represented by the reaction:



and it is concluded that a_{C} is increasing with time. At the equilibrium value of $a_{\text{C}} \approx 1$ calculated for scale-alloy equilibrium (Eqs [10.3]–[10.7]), assuming graphite not to precipitate, overall carbon concentrations of 6.8 and 9.1 at.% are predicted from ThermoCalc for equilibrated 9% and 12% Cr steels. Although the boundary carbon concentrations shown in Fig. 10.20 are approaching equilibrium, they are still far removed from that state.

A full account of the nonsteady-state carbon reaction at these low temperatures requires a description of its permeation through the oxide scale, its transfer from oxide to metal and its penetration and carburisation of the alloy.

Despite the nonsteady-state conditions apparent in Fig. 10.20, carburisation depths increased according to parabolic kinetics after an initial period of more rapid reaction (Fig. 10.21). The rate at which carbon enters the steel and partitions between matrix and precipitate phases in such a way as to yield parabolic penetration kinetics is of interest.

The simplest hypothesis is that the rate of carbon entry is proportional to the difference between the actual concentration of solute carbon, $N_{\text{C}}^{(s)}/V$, and the equilibrium value, $N_{\text{C}}^{\text{eq}}/V$, with V the alloy molar volume. Then the boundary condition is provided by:

$$\alpha \left(N_{\text{C}}^{\text{eq}} - N_{\text{C}}^{(s)} \right) = -D \frac{\partial N_{\text{C}}}{\partial x} \quad [10.14]$$

where α is a rate constant (units: cm s⁻¹). When $N_{\text{C}}^{(s)}$ is small compared with N_{C}^{eq} , the rate of carbon uptake is approximately constant.

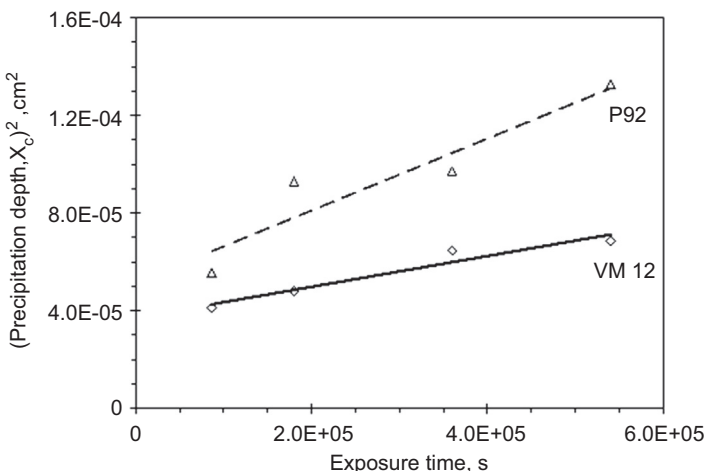


FIGURE 10.21 Parabolic plots for carburisation depth (derived from GDOES profiles) as a function of time in P92 and VM12 during exposure at 550°C in Ar-50% CO₂. $X_c = 0$ corresponds to scale/steel interface. Reprinted from D.J. Young, P. Huczkowski, T. Olszewski, T. Hüttel, L. Singheiser, W.J. Quadakkers, *Corros. Sci.*, 88 (2014) 161, with permission from Elsevier.

Nonsteady-state diffusion within the steel is complicated by the loss of a large fraction of carbon as additional precipitate. Once precipitated, this carbon cannot diffuse, and the usual diffusion equation [1.24] must be modified to account for the additional loss of solute. For simplicity, we assume an essentially instantaneous reaction and achievement of local equilibrium as described by the lever rule in molar units

$$N_{\text{CrC}_v} = \frac{N_{\text{Cr}}^{(0)} - N_{\text{Cr}}}{N_{\text{Cr}}^P - N_{\text{Cr}}} \quad [10.15]$$

where N_{Cr}^P and N_{Cr} refer to local values in the precipitate and matrix phases. As before, $N_{\text{Cr}}^{(0)}$ denotes the original alloy chromium content. Chromium and carbon matrix concentrations are related via the equilibrium [10.13], which can be expressed using the solubility product K_{sp}

$$K_{\text{sp}} = N_{\text{Cr}}^7 N_{\text{C}}^3 \quad [10.16]$$

where dissolution of iron by the carbide is ignored. Recalling that the concentration $C_i = N_i/V$, and approximating the total concentration of carbon, C_{C}^T , by ignoring carbon dissolved in the matrix,

$$C_{\text{C}}^T = \frac{\nu N_{\text{CrC}_v}}{V} \quad [10.17]$$

it is found from Eqs [10.15]–[10.17] that

$$\frac{C_C^T}{C_C^M} = \frac{\nu N_{\text{Cr}}^{7/3}}{K_{\text{sp}}^{1/3}} \frac{N_{\text{Cr}}^{(0)} - N_{\text{Cr}}}{N_{\text{Cr}}^P - N_{\text{Cr}}} \quad [10.18]$$

Here the superscripts M and T refer to the matrix (solute) and overall concentrations. If the variation of N_{Cr} with position in the diffusion zone is ignored, then [10.18] is simplified as

$$C_C^T = \beta C_C^M \quad [10.19]$$

Using a calculated phase diagram, and modelling the steels as simple Fe-Cr-C ternaries, it is found that $\beta \approx 4 \times 10^4$ for the 12% Cr steel, but $\approx 2.5 \times 10^4$ for the 9% Cr steel. As the carbon activity at the oxide-alloy interface increases with time, the boundary value solute concentration, C_C^M , increases by a small amount, but the extent of precipitation, as reflected by C_C^T , increases greatly. This explains the observations of rapidly increasing carbon concentrations (Fig. 10.20) combined nonetheless with approximately steady-state parabolic kinetics of penetration (Fig. 10.21).

For this situation, Fick's second law [2.138] is replaced by

$$\frac{\partial C_C^M}{\partial t} = D \frac{\partial^2 C_C^M}{\partial x^2} - \frac{\partial C_C^T}{\partial t} \quad [10.20]$$

where again the concentration of carbon trapped in precipitates is approximated as C_C^T . Substitution from [10.19] into [10.20] leads to

$$\frac{\partial C_C^M}{\partial t} = \frac{D}{\beta + 1} \frac{\partial^2 C_C^M}{\partial x^2} \quad [10.21]$$

which has the usual form, but a smaller diffusion coefficient. Consequently, the usual mathematical solutions apply, explaining the qualitative success of the Wagner description, Eq. [10.8].

If movement of the scale-alloy interface can be neglected, the carbon diffusion problem is described by the combination of Eqs [10.14] and [10.21]. The solution for a semi-infinite alloy sample initially containing carbon concentration C_1 is [56]

$$\frac{C_C - C_1}{C_C^{\text{eq}} - C_1} = \operatorname{erfc} \frac{x}{2\sqrt{Dt}} - \exp(hx + h^2Dt) \times \operatorname{erfc} \left\{ \frac{x}{2\sqrt{Dt}} + h\sqrt{Dt} \right\} \quad [10.22]$$

where $h = \alpha/D$. The interfacial concentration $C_C^{(s)}$, at $x = 0$ is then

$$\frac{C_C^{(s)} - C_1}{C_C^{\text{eq}} - C_1} = 1 - \exp(h^2Dt) \times \operatorname{erfc}(h\sqrt{Dt}) \quad [10.23]$$

and $C_C^{(s)}$ is asymptotic to C_C^{eq} , as required. The rate at which the total amount of carbon in the sample, M_C , increases is found to be

$$M_C = \frac{C_C^{eq} - C_1}{h} \left\{ \exp(h^2 Dt) \times \operatorname{erfc}(h\sqrt{Dt}) - 1 + 2h\sqrt{\frac{Dt}{\pi}} \right\} \quad [10.24]$$

Eq. [10.23] has been tested [24] by comparing its predictions with experimental results for interfacial total carbon concentrations, recognising from Eq. [10.19] that the ratio of matrix concentrations $C_C^{(s)}/C_C^{eq}$ equals that of measured total concentrations. The results are shown in Fig. 10.22, where C_s is the instantaneous value of total carbon concentration at the surface, C_0 its equilibrium value, and C_1 the initial carbon content in the alloy. Here the value of $h = \alpha/D$ was adjusted to yield $(C_s - C_1)/(C_0 - C_1)$ equal to the quantities measured after 150 h, and values of C_0 were calculated as before at 6.8 and 9.1 at.% for the 9% and 12% Cr steels, respectively. The shape of the calculated curves is seen to be in good agreement with the measurement, providing support for the kinetic model of Eqs [10.14] and [10.20].

Proceeding in this way, it was found that $\alpha = 1.6 \times 10^{-6} \text{ cm s}^{-1}$ for P92 and $3.5 \times 10^{-6} \text{ cm s}^{-1}$ for VM12, the rate of carbon transfer across the oxide-alloy interface being greater for the latter. The authors suggested that the difference in the surface transfer rate was due to the different chemical composition of the steels, leading to differing catalytic efficiencies for the Boudouard reaction.

The role played by the kinetics of the Boudouard reaction has been considered by Rouillard et al. [26]. If reaction [10.2] is considered slow, and the reverse process significant, then the net reaction rate, r_B , can be written

$$r_B = k_2(p_{CO}^{in})^2 - k'_2 a_C p_{CO_2}^{in} \quad [10.25]$$

where the superscript *in* denotes the value at the oxide-alloy interface, and k_i , k'_i the forward and reverse rate constants. Rouillard evaluates p_{CO}^{in} and $p_{CO_2}^{in}$ from mass balance, omitting the contribution of the Boudouard reaction. Assuming the arrival of CO_2 to be via diffusion control through the oxide scale and its consumption to be through the oxidation reaction



leads to

$$\frac{dp_{CO_2}^{in}}{dt} = \frac{D_{CO_2} (p_{CO_2}^{out} - p_{CO_2}^{in})}{X} - k_{26} p_{CO_2}^{in} \quad [10.27]$$

where k_{26} is the rate constant for reaction [10.26], $p_{CO_2}^{out}$ the ambient CO_2 partial pressure and D_{CO_2} the diffusion coefficient for CO_2 in the nanoporous scale. In the steady state, $p_{CO_2}^{in}$ is time independent, and given by

$$p_{CO_2}^{in} = \frac{p_{CO_2}^{out}}{(1 + k_{26}X/D_{CO_2})} \quad [10.28]$$

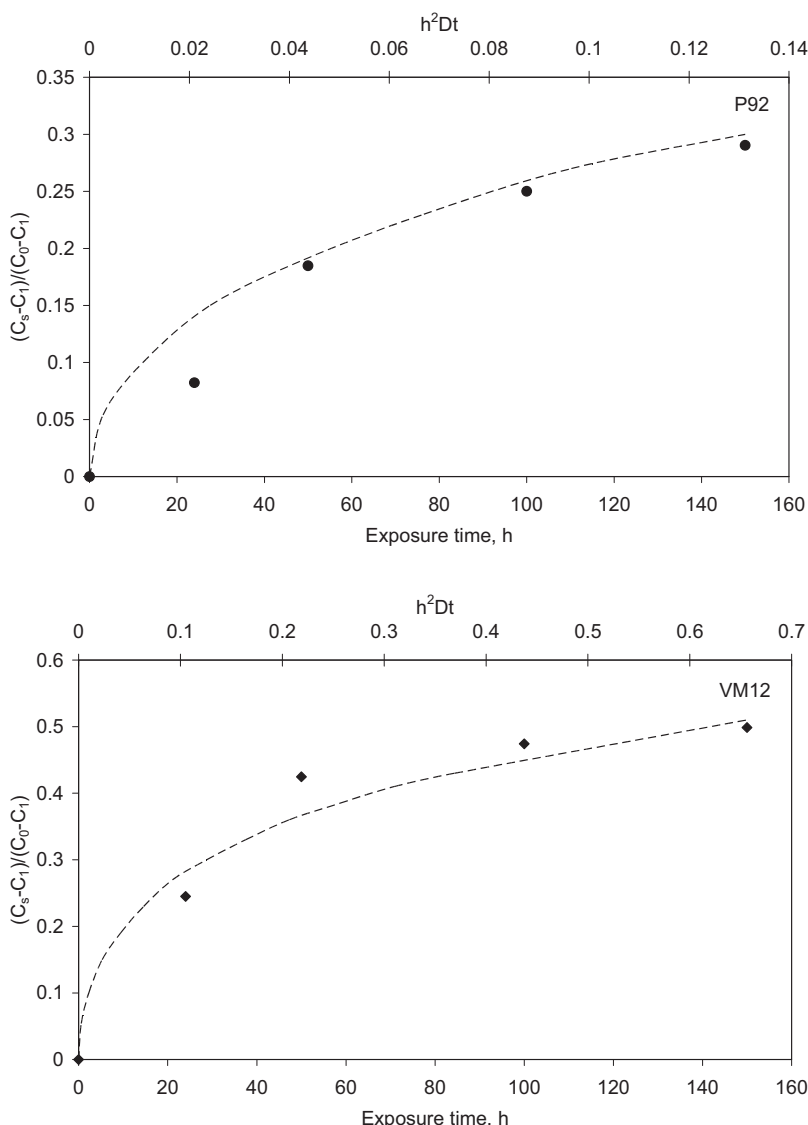


FIGURE 10.22 Values of $(C_s - C_1)/(C_0 - C_1)$ calculated from Eq. [10.24] as a function of time compared with experimental data for P92 and VM12. Upper axis shows values for h^2Dt . Reprinted from D.J. Young, P. Huczkowski, T. Olszewski, T. Hüttel, L. Singheiser, W.J. Quadakkers, Corros. Sci., 88 (2014) 161, with permission from Elsevier.

Similarly, if CO is generated by reaction [10.26] and lost via diffusion out through the scale, then

$$p_{\text{CO}}^{\text{in}} = \frac{k_{26}X p_{\text{CO}_2}^{\text{in}}}{D_{\text{CO}}} \quad [10.29]$$

Here the negligibly small value of $p_{\text{CO}}^{\text{out}}$ has been approximated to zero. Substitution from [10.28] and [10.29] into [10.25] then yields

$$r_B = k_2 \left(\frac{k_{26}X}{D_{\text{CO}}(1 + k_{26}X/D_{\text{CO}})} \right)^2 \left(p_{\text{CO}_2}^{\text{out}} \right)^2 - k'_2 \frac{a_C}{(1 + k_{26}X/D_{\text{CO}_2})} p_{\text{CO}_2}^{\text{out}} \quad [10.30]$$

for the net rate of the carbon production process.

This purely kinetic model succeeds in describing the increased amount of carbon deposition observed at higher p_{CO_2} values, and the increase with time in the rate of carbon uptake relative to that of oxygen. The latter effect is attributed to the increase with time in p_{CO} beneath the scale predicted from Eqs [10.28] and [10.29] and the scaling rate equation, $X^2 = 2k_p t$.

In fact, the model predicts that $b = p_{\text{CO}}/p_{\text{CO}_2}$ increases with time, as seen in Eq. [10.29]. This implies (Eq. [10.3]) that $(p_{\text{O}_2})_{\text{eq}}$ at the scale-alloy interface decreases with time, which is inconsistent with the reported [25] steady-state parabolic scaling kinetics. Nonetheless, Boudouard reaction rates are certainly slow, a fact which needs to be taken into account in any description.

An alternative treatment can be formulated on the basis that oxide scale-alloy equilibrium controls $(p_{\text{O}_2})_{\text{eq}}$ and therefore $b = p_{\text{CO}}/p_{\text{CO}_2}$ at a fixed value, but the carbon activity, a_C , only slowly approaches equilibrium. In the early stages of reaction, after steady-state scaling is established, the alloy undergoes nonsteady-state carburisation, but no carbon is deposited within the scale. Under these conditions, carbon is produced at the scale-alloy interface according to [10.25] [26] and is drained away into the alloy as described by [10.14] [24]. The carbon activity changes with time as a result:

$$\frac{da_C}{dt} = k_2 (p_{\text{CO}}^{\text{in}})^2 - k'_2 p_{\text{CO}_2}^{\text{in}} a_C - \alpha (a_C^{\text{eq}} - a_C) \quad [10.31]$$

where carbon activity has replaced concentration in [10.14]. Here a_C^{eq} is the equilibrium value corresponding to Eq. [10.7], achieved when the Boudouard reaction attains equilibrium.

When $a_C = a_C^{\text{eq}}$, da_C/dt becomes zero, and [10.31] yields

$$a_C^{\text{eq}} = \frac{k_2 (p_{\text{CO}}^{\text{in}})^2}{k'_2 p_{\text{CO}_2}^{\text{in}}} \quad [10.32]$$

Since, by definition,

$$\frac{k_2}{k'_2} = K_2 \quad [10.33]$$

[Eq. \[10.32\]](#) is seen to be equivalent to the Boudouard equilibrium [\[10.4\]](#). The kinetics of approach to the equilibrium state are found by integrating [\[10.31\]](#) to obtain

$$a_C = a_C^{\text{eq}}[1 - \exp(-\beta t)] \quad [10.34]$$

where the condition $a_C = 0$ at $t = 0$ has been used, and

$$\beta = \frac{k'_2}{b} p_{\text{CO}_2}^{\text{in}} - \alpha \quad [10.35]$$

[Eq. \[10.34\]](#) is seen to be asymptotic to $a_C = a_C^{\text{eq}}$.

Nonsteady-state carburisation of substrate metal according to [Eq. \[10.14\]](#) is thus seen to be consistent with a Boudouard reaction which only slowly approaches equilibrium. This description is only valid when the carbon produced is dissolved into the metal, as described by [\[10.31\]](#), and cannot apply when elemental carbon is deposited within the oxide. It is likely that at temperatures and pressures producing the high values of a_C required for deposition, a metal carburisation process precedes the onset of deposition, as the interfacial carbon activity builds up to the critical level required to nucleate solid carbon.

Once carbon deposition commences, the properties of the oxide scale are altered by mechanical disruption. Under these conditions, CO_2 entry is presumably facilitated, and the oxidation process [\[10.26\]](#) proposed by Rouillard [\[26\]](#) is likely to control scaling.

Whilst the thermodynamics and kinetics of carbon uptake within and beneath iron oxide scales are reasonably well-described, the mechanism whereby carbon permeates through dense, compact iron oxide layers remains unknown.

10.5.3 Carbon Penetration of Chromia Scales

As noted earlier, although chromia scales are very much more protective than iron oxides against carbon entry, nonetheless carburisation occurs beneath Cr_2O_3 ([Fig. 10.7](#)). An investigation [\[60\]](#) of the effects of CO_2 on the microstructure of chromia scales, and the location of carbon within them, provides information on the mechanism.

Specimens of Fe-20Cr reacted with flowing $\text{Ar}-20\text{O}_2$ and $\text{Ar}-20\text{CO}_2$ at 650°C developed the scale microstructures shown in [Fig. 10.23](#). Analysis by SAD showed both to be single-phase Cr_2O_3 . Scale thickness measurements after different reaction times show in [Fig. 10.24](#) that reaction in CO_2 was faster than in O_2 . Parabolic rate constants are shown in [Table 10.4](#), along with measured average oxide grain sizes.

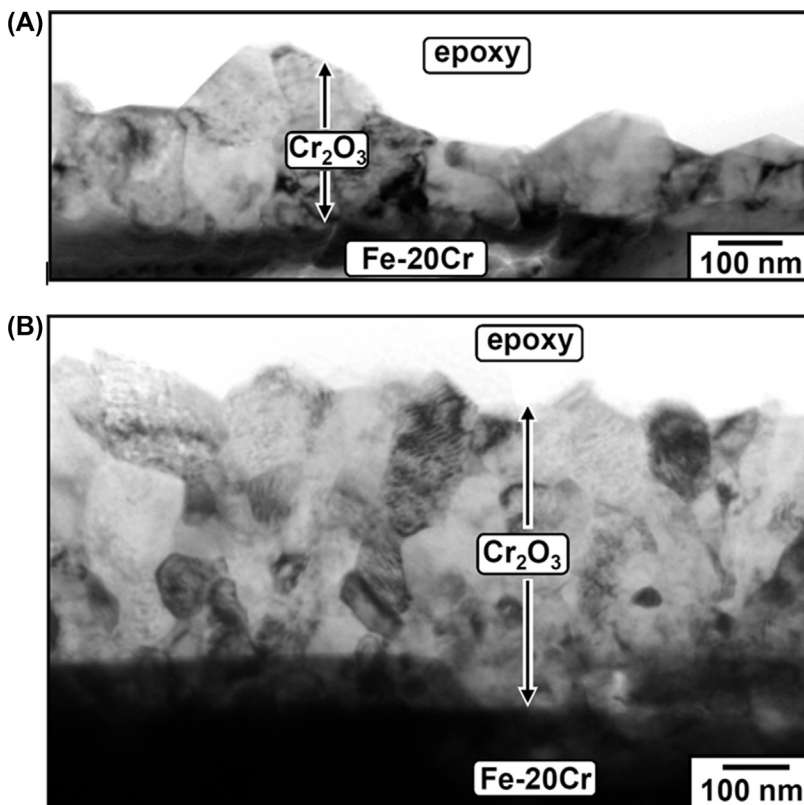


FIGURE 10.23 TEM bright field images of Cr_2O_3 scale cross-sections grown on Fe-20Cr at 650°C: (A) in Ar-20 O_2 for 24 h; (B) in Ar-20 CO_2 for 120 h. Reprinted from D.J. Young, T.D. Nguyen, P. Felfer, J. Zhang, J.M. Cairney, *Scripta Mater.* 77 (2014) 29, with permission from Elsevier.

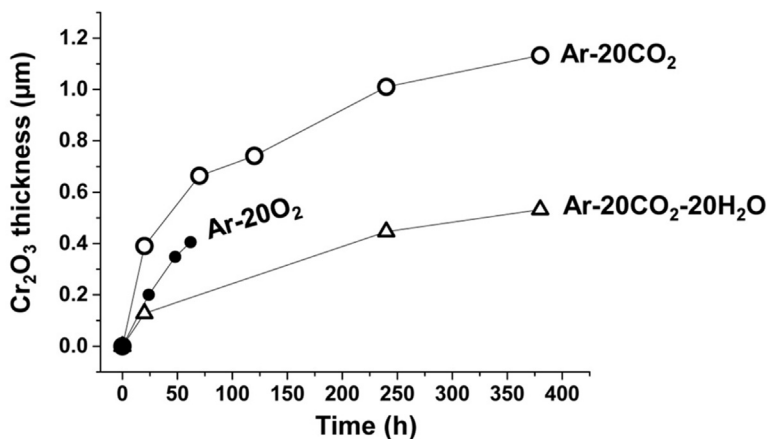


FIGURE 10.24 Chromia scale growth kinetics on Fe-20Cr at 650°C.

TABLE 10.4 Chromia Scales Grown on Fe-20Cr at 650°C [60]

Reaction Gas (Time)	Thickness (nm)	Grain Shape and Size (nm)	$(k_p/\text{cm}^2 \text{ s}^{-1})^b$
Ar-20O ₂ (24 h)	200 ± 40	Equiaxed: 170 ± 10	$(3.7 \pm 0.4) \times 10^{-15}$
Ar-20CO ₂ (120 h)	720 ± 200	Columnar ^a : 100 ± 10	$(4.6 \pm 0.5) \times 10^{-15}$
Ar-20O ₂ (24 h) + Ar-20CO ₂ (70 h)	Outer: 350 ± 140 Inner: 510 ± 150	Equiaxed: 200 ± 15 Equiaxed: 90 ± 10	

^aColumn width.
^bFrom Fig. 10.24.

Diffusion in Cr₂O₃ is predominantly via grain boundaries at these temperatures [61], and the Hart Eq. [3.113] for mixed lattice and boundary diffusion is adequately approximated by

$$D_{\text{eff}} = fD_b \quad [10.36]$$

where again f is the fraction of diffusion sites within the boundaries. For columnar grains of square cross-section,

$$f = \frac{2d}{D_t} \quad [10.37]$$

with d the boundary width and D_t the grain size, and if D_t is constant with time,

$$k_p \propto \frac{1}{D_t} \quad [10.38]$$

The data in Table 10.4 yield $D_t^{\text{CO}_2}/D_t^{\text{O}_2} = 0.6 \pm 0.1$ and $k_p^{\text{O}_2}/k_p^{\text{CO}_2} = 0.8 \pm 0.2$. Agreement with [10.38] is satisfactory, confirming that chromia scale growth in CO₂ is supported by grain boundary diffusion.

Etching revealed internal carbides on alloy grain boundaries after exposure to CO₂. These were identified by SAD as M₂₃C₆ (Fig. 10.2). Internal carbide precipitation depth increased with exposure time in Ar-20CO₂ (Fig. 10.6), showing that carbon penetrates the chromia scale and continues to pass through it into the alloy. A two-stage experiment confirmed this conclusion. A single alloy specimen was exposed in Ar-20O₂ for 24 h, the gas supply switched without change in temperature, and exposure continued in Ar-20CO₂ for a further 70 h. The results in Fig. 10.25A demonstrate clearly that carbon species from the gas passed through the pre-existing chromia scale, carburising the alloy beneath.

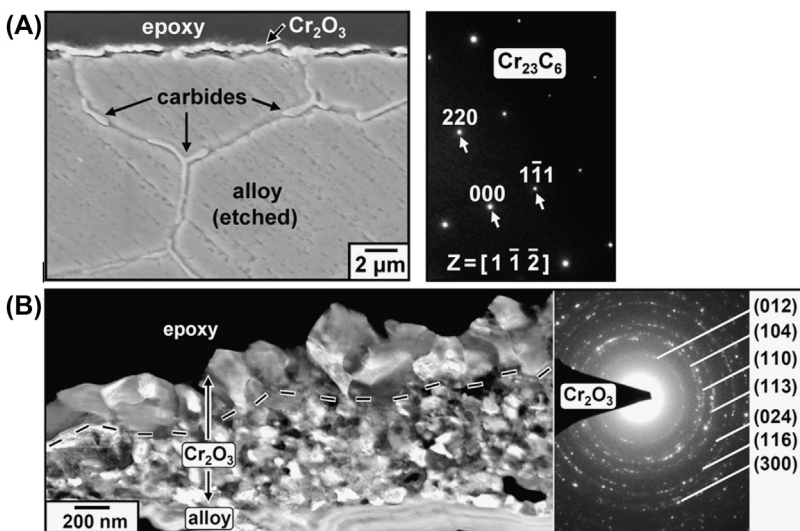


FIGURE 10.25 Reaction products for Fe-20Cr after 24 h in Ar-20O₂ followed by 70 h in Ar-20CO₂ at 650°C: (A) SEM view showing internal carburisation, SAD identifies M₂₃C₆; (B) STEM dark field image showing two-layered chromia scale. *Reprinted from D.J. Young, T.D. Nguyen, P. Felfer, J. Zhang, J.M. Cairney, Scripta Mater. 77 (2014) 29, with permission from Elsevier.*

External scale development is also altered by the two-stage experiment, which led to the two-layered scale shown in Fig. 10.25B. Scale layer thicknesses developed in the two-stage experiment are compared with those grown in CO₂ alone or O₂ alone in Table 10.4, along with average grain sizes. As seen in Table 10.4, the outer layer resulting from the two-stage reaction corresponds approximately in thickness and grain size to the single layer formed in the first stage of reaction in oxygen alone. Evidently the second (CO₂) stage of reaction produced fine-grained oxide beneath the first-formed layer, reflecting inward diffusion of oxidant.

Tracer diffusion experiments [62] show that at 1050°C, chromia scales grow in oxygen by outward metal diffusion, but in H₂/H₂O gas, they grow mainly by inward oxidant transport. A similar pattern of behaviour is apparent at the lower temperature of 650°C used here, where the use of CO₂ leads to production of finer oxide grains, faster scaling and inward scale growth. Obviously, these changes would not result if the mobile species within the scale were simply oxygen ions in both cases. Since, moreover, the CO₂ reaction leads to carburisation as well as oxidation, inward transport of a compound species such as molecular CO₂ is indicated. This deduction that CO₂ transports along oxide grain boundaries is supported by the observation that the presence of carbon alters the oxide grain size (Fig. 10.23). The hypothesis has been tested using atom probe tomography.

Atom probe tips can be FIB milled from precise locations within a thin scale. As seen in the example of Fig. 10.26A, oxide grain boundaries are captured in the tips and can therefore be analysed. The reconstructed three-dimensional image in Fig. 10.26B has been modified by removing 99% of Cr and O atoms, so as to enhance the visibility of impurity species. It clearly shows carbon decorating grain boundaries within the Cr_2O_3 . A section through the scale-alloy interface shown in Fig. 10.27 reveals carbon enrichment at the scale-alloy interface and at a curved oxide-oxide grain boundary meeting the alloy surface. Thus it is established that carbon penetrates chromia scales via their grain boundaries.

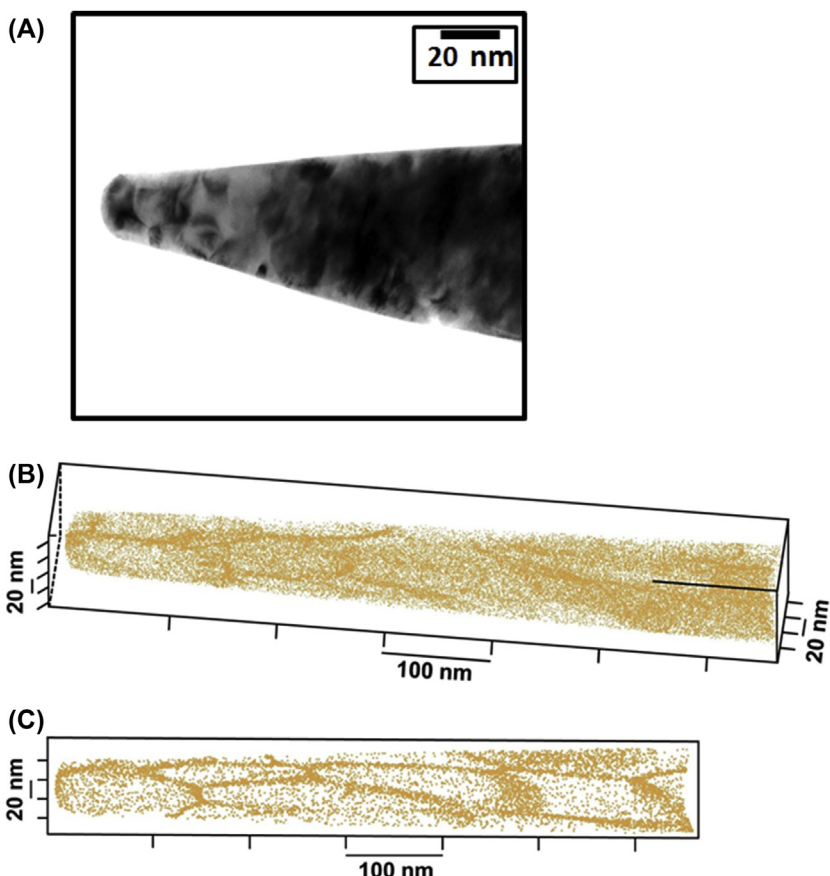


FIGURE 10.26 (A) Bright field TEM image of tip FIB milled from chromia scale for atom probe tomography; (B) three-dimensional representation of carbon distribution in fine-grained chromia scale, with 99% of atoms in bulk oxide removed; and (C) two-dimensional longitudinal slice through (B). Oxide grown on Fe-20Cr in Ar-20CO₂ at 650°C.

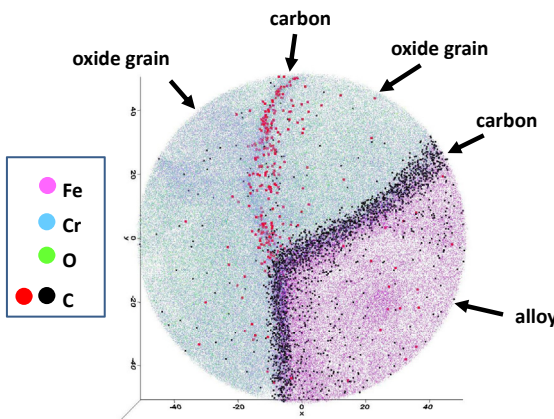
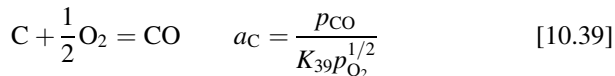


FIGURE 10.27 Atom probe tomographic section through chromia scale-alloy interface/oxide grain boundary junction on Fe-20Cr reacted with Ar-20CO₂ at 650°C.

The chemical state of the carbon in oxide grain boundaries is not revealed by the APT results. Elemental carbon would be thermodynamically possible at the low oxygen potentials expected within chromia scales but would presumably contribute very little to carbon diffusion. Carbon surface concentrations were measured [60] as 5.6 ± 0.7 and 5.2 ± 0.8 atom nm⁻² on the scale-alloy interface and oxide grain boundary, respectively. These values are much lower than that expected for a carbon monolayer on the basis that a graphene sheet contains about 40 atom nm⁻², and the carbon must therefore be present in another form.

Standard thermodynamic data (Table 2.1) show the minimum oxygen potential within the oxide to be $p_{O_2} = 1.4 \times 10^{-32}$ atm at the scale-metal interface, where it is controlled by the Cr/Cr₂O₃ equilibrium. This corresponds via [10.2] to $p_{CO}/p_{CO_2} = 2.8 \times 10^4$. For $a_C < 1$, the equilibrium



implies a value of $p_{CO} < 10^{-5}$ atm, and consequently, $p_{CO_2} < 3.4 \times 10^{-10}$ atm. Whilst consistent with the mechanism deduced earlier of transport by carbon oxide species, direct evidence of the oxidation state is desirable.

10.6 EFFECTS OF OTHER ALLOY AND GAS COMPONENTS

Real engineering alloys contain multiple minor components, added for processing reasons or microstructure control. As seen in Section 7.6, these additions can strongly modify alloy oxidation behaviour. It has been reported [27] that commercial 9Cr steels are more resistant to CO₂ than binary Fe-Cr

TABLE 10.5 Calculated Coal-Fired Furnace Gas Compositions (vol.%)

Species	Lignite [74]		High S (2%) Coal [73]	
	Oxyfuel	Air Fired	Oxyfuel	Air Fired
N ₂	4.8	71.3	4.5	74.2
O ₂	1.9	2.5	3.3	3.3
CO ₂	58.9	15.3	61.2	13.9
H ₂ O	31.8	10.0	30.3	8.4
SO ₂	0.49	0.13	0.7	0.2

alloys containing 10–13.5% Cr. The effects of minor alloy additives on CO₂ corrosion are therefore of potential interest.

Corrosion by CO₂ in oxyfuel combustion gas takes place in an atmosphere which also contains water vapour, residual oxygen and SO₂ (typical composition in Table 10.5). The effects of the secondary oxidants need also to be considered.

10.6.1 Silicon Effects

The benefits of adding silicon in improving the oxidation resistance of steels in various gases (H₂O, H₂-H₂O, CO₂-CO, O₂ and air) have been long known. A dense and slow-growing SiO₂ layer formed at the Cr-rich oxide scale-alloy interface contributes to the improved oxidation resistance of Cr steels [63–66]. As shown in Section 9.8, such a layer can sometimes protect heat-resisting alloys against carburisation in hydrocarbon gases. The same benefits can be achieved in the case of CO₂ corrosion [67].

Small additions of silicon have strong effects on the weight uptake kinetics of model alloys Fe-9Cr, Fe-20Cr and Fe-20Ni-20Cr exposed to Ar-20CO₂ at 818°C, as seen in Fig. 10.28. Silicon-free alloys all underwent internal carburisation. Silicon additions completely suppressed carburisation in the 20Cr alloys at levels of 0.1% and above, and in the 9Cr alloy at levels of 0.2% and above. Prevention of carburisation was associated with the formation of a thin layer of amorphous silica at the scale-alloy interface (Fig. 10.29). Evidently, this layer functions as a very effective barrier to carbon transmission.

Silica-free alloys developed scales which were thick and iron-rich on Fe-9Cr, but thin Cr₂O₃ on Fe-20Cr. The Fe-20Cr-20Ni alloy formed a protective Cr₂O₃ scale at an early stage of oxidation, but developed a thick Fe₃O₄ scale and an internal oxidation zone of (FeCr₂O₄ + FeNi₃) at longer reaction times.

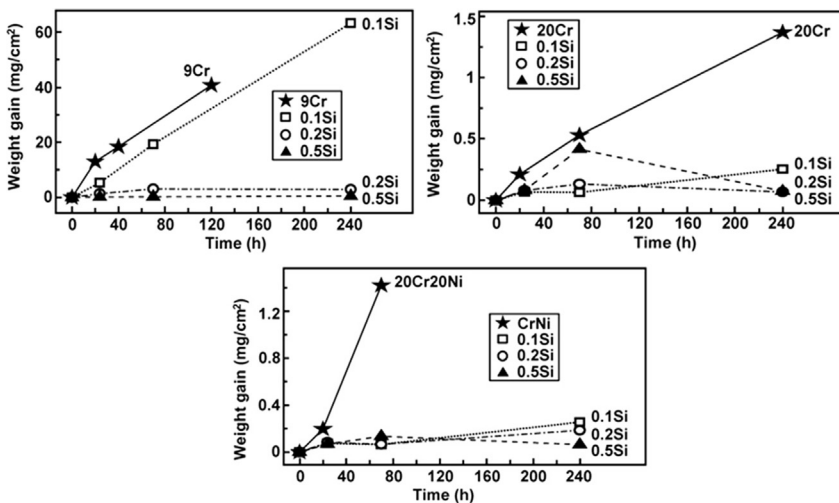


FIGURE 10.28 Weight uptake kinetics observed for model alloys reacted with Ar-20CO₂ at 818°C [67]. With kind permission from Springer Science and Business Media.

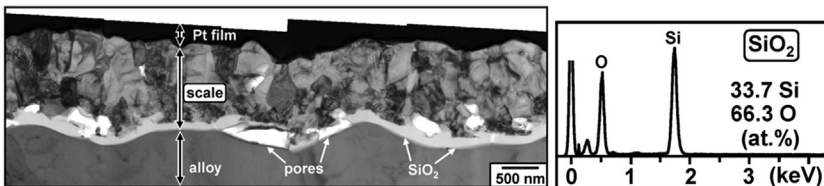


FIGURE 10.29 Bright field TEM image of scale grown on Fe-20Cr-0.2Si in Ar-20CO₂ at 818°C, with EDAX analysis of inner oxide layer [67]. With kind permission from Springer Science and Business Media.

In the absence of silicon, the ability of an alloy to selectively oxidise Cr and form a protective chromia scale is determined by the concentration and diffusion coefficient of chromium (Section 5.4). In the high diffusivity ferritic alloys, clearly a chromium level of 9% was insufficient, but 20% was enough. The same concentration in the austenitic Fe-20Cr-20Ni was inadequate, because of the lower alloy diffusion coefficient. Additions of Si to the low chromium ferritic Fe-9Cr and the high chromium austenitic Fe-20Cr-20Ni had a profound effect on each alloy's ability to passivate in CO₂.

A Cr₂O₃ layer developed on ferritic Fe-(9,20)Cr-0.2Si and austenitic Fe-20Cr-20Ni-0.2Si alloys, regardless of the different D_{Cr} values in ferrite and austenite. It may therefore be concluded that the enhanced oxidation resistance of Si-bearing alloys was due mainly to the formation of an additional protective SiO₂ layer at the scale-alloy interface, where it slowed Cr₂O₃ growth, resulting in less chromium depletion in the subsurface zone. The silica layer

must slow outward iron diffusion to an even greater extent, allowing chromia to develop on the Fe-9Cr alloy. Knowledge of metal diffusion coefficients in amorphous silica would be of value in understanding more fully the effects of the silica layer.

The silica layer effect may account for the improved performance [27] of commercial alloys, which all contain silicon (Table 10.2), over that of simple binary Fe-Cr alloys.

Silica layer formation is only possible because the outer chromia layer reduces the oxygen activity, favouring external silica growth over internal precipitation (Section 7.4.5). Reaction of binary Fe-Si alloys in CO₂ leads to internal oxidation of the silicon, and little benefit to alloy corrosion resistance is achieved [68].

10.6.2 Manganese Effects

It has been reported [69] that the MnCr₂O₄ spinel is impermeable to carbon. If such a layer can be formed during exposure to CO₂, alloy manganese additions could be potentially useful in preventing carburisation. This expectation is met in the case of Fe-20Cr-(1,2)Mn, where a distinct outer scale layer of spinel develops during reaction with Ar-20CO₂ at 818°C, and internal carburisation is completely suppressed [39]. Overall weight uptake rates during corrosion in Ar-20CO₂ are also decreased.

For Fe-20Cr-(1,2)Mn, the presence of Mn increases oxidation resistance in Ar-20CO₂ to a certain extent by forming spinel scale layers [31,39]. It has been reported long ago [70] that this spinel layer increases the oxidation resistance in air. One factor leading to this improvement is the changed boundary conditions governing chromia layer growth [71]. In the CO₂ reaction, the addition of 1Mn to Fe-20Cr had a small effect, but the 2Mn addition showed a significant improvement. The chromia scale formed on Fe-20Cr-2Mn in CO₂ is only slightly thicker than in air, but significantly less than that on Fe-20Cr in CO₂. It is concluded on this basis that the accelerating effect of carbon on transport in the chromia scale on other Fe-20Cr alloys is offset by the behaviour of the manganese spinel layers. Manganese incorporation into the scale clearly has an important role in slowing metal and/or oxygen diffusion, as well as in blocking carbon penetration. This is consistent with the conclusion reached above that scale penetration by CO₂ plays a major role in the mass transport supporting oxidation. Because less Cr was consumed in forming the scale on Fe-20Cr-2Mn, lower porosity was developed at the scale-alloy interface. Thus Mn additions to Fe-20Cr are beneficial in several ways for corrosion resistance in CO₂.

The beneficial effects of alloy silicon and manganese additions have been defined at only one temperature, 818°C. However, old reports [41,72] on carbon deposition under gas-cooled nuclear reactor conditions note that a

condition for carbon deposition to occur is a low silicon content in the steel. There is a need to determine critical levels of silicon and manganese required for enhanced resistance to CO₂ corrosion over a range of temperatures and gas compositions.

10.6.3 Gas Composition Effects

Supercritical CO₂ used as a heat transfer medium and working fluid in a turbine cycle will be of high purity. However, the CO₂ present in oxyfuel combustion environments is accompanied by other species. Water vapour derives from combustion of volatile components in the coal, and SO₂ derives from the coal mineral content. In addition, a small excess of oxygen is present in order to achieve full fuel utilisation.

Sulphur levels in coal vary considerably with geographic location. However, for a given coal, gas phase SO₂ levels are higher in the oxyfuel process than in air combustion, firstly because of the absence of N₂ diluent, and secondly because a fraction of the flue gas is recycled and used to control combustion temperatures. Calculations [73,74] of furnace gas compositions yield the results in Table 10.5, where air firing and oxyfuel firing are compared for two different coals. Minor differences arise from different assumptions as to the air (or oxygen) to fuel ratio, but the elevated levels of water vapour and SO₂ in oxyfuel gas are clear. Overall, oxyfuel gas compositions have been shown [75] to be more corrosive than air for a variety of chromia-forming alloys and low alloy steels at 650°C.

10.6.4 Water Vapour Effects

The ways in which water vapour can effect oxide scaling are discussed in detail in Chapter 11. Studies of the combined effects of H₂O(g) and CO₂ on alloy corrosion are limited, and the results to date fail to yield a self-consistent picture. Thus, for example, reaction at 650°C of binary Fe-Cr alloys containing up to 13.5% Cr was found [27,76] to vary with gas composition in the sequence: rate (CO₂-30H₂O) > rate (Ar-30H₂O) > rate (Ar-30CO₂) > rate (air). The same sequence was reported for the steels T91, T92 and P92. At 550°C, however, the martensitic steels P92 and VM12 were found [22,77] to react at different rates in the sequence: rate (Ar-50CO₂) > rate (CO₂-30H₂O) > rate (Ar-50H₂O) > rate (air). Obviously, the temperatures for the two sets of results are different, but just how this leads to the very different results is unclear.

A model alloy Fe-22Cr was found [76] to passivate in CO₂-30H₂O at 650°C, whereas an Fe-25Cr alloy was observed [8] to nucleate iron-rich oxide nodules, converting a passive chromia scale into a fast-growing iron-rich one in both Ar-20CO₂ and Ar-20CO₂-20H₂O at the same temperature. Until a broader set of results, including (in particular) more detailed kinetic

observations, is available, these apparent inconsistencies cannot be resolved. Nonetheless, the negative effect of water vapour is generally observed and can fruitfully be discussed.

For alloys containing low to intermediate chromium levels, breakaway oxidation in CO_2 is invariably observed, and the interaction of iron oxides with the gas phase is important. As discussed in [Section 10.3](#), the relatively slow reaction of CO_2 at the iron oxide scale surface can fail to keep pace with the rapid rate of outward iron diffusion through the scale, resulting in an inability to achieve local oxide-gas equilibrium, and to convert surface oxides to the higher oxidation states expected. Water vapour reacts faster at the surface [6], allowing formation of the higher iron oxides observed in $\text{CO}_2\text{-H}_2\text{O}$ gas mixtures [76,78]. Initial scaling follows fast linear kinetics in these gas mixtures, and thicker scales are produced before steady-state conditions are achieved at the scale-gas interface.

Of greater importance is the fact that higher alloy chromium levels are required to resist breakaway when significant amounts of $\text{H}_2\text{O(g)}$ are present in the CO_2 . Analysis of this phenomenon is complicated by the seemingly random nature of the nodule nucleation events which initiate breakaway ([Fig. 10.5](#)). Grain orientation has been shown to affect the nature of the oxide formed on binary Fe-Cr alloys [79,80]. It is seen also to affect nodule nucleation of an austenitic chromia former in [Fig. 10.30](#). Nucleation rates assessed [8] from observations of surface area fractions of iron-rich oxide formed on chromia-forming alloys in wet CO_2 mixtures are shown in

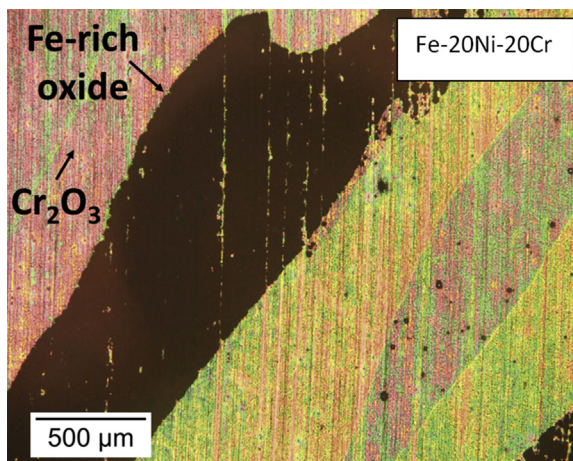


FIGURE 10.30 Surface view of Fe-20Ni-20Cr after 120 h in $\text{Ar-20CO}_2\text{-20H}_2\text{O}$ at 650°C . Reprinted from T. Gheno, D. Monceau, D.J. Young, *Corros. Sci.*, 77 (2013) 246, with permission from Elsevier.

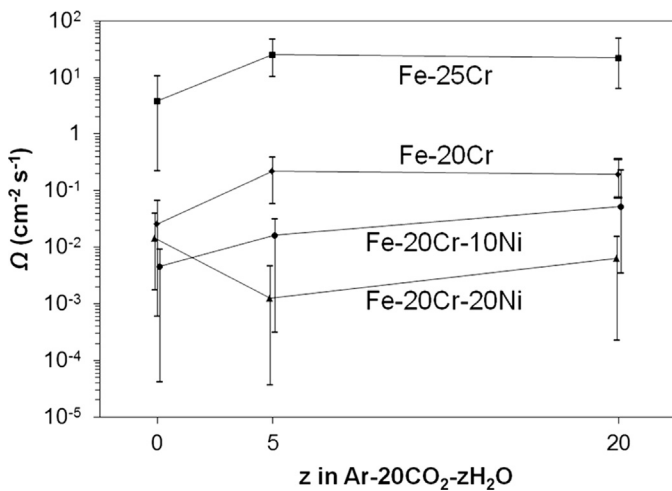


FIGURE 10.31 Nucleation rates assessed from surface area fraction measurements after exposure at 650°C. Reprinted from T. Gheno, D. Monceau, D.J. Young, *Corros. Sci.*, 77 (2013) 246, with permission from Elsevier.

Fig. 10.31. The assessment is based on the application of Evans' theory of nucleation and spreading on a plane surface [81], which leads to

$$\theta = 1 - \exp(-\pi \Omega k_l t^2) \quad [10.40]$$

where θ is the area fraction of iron-rich oxide, Ω the number of nuclei formed per unit of surface area and time, or nucleation rate, and k_l the lateral parabolic rate constant for nucleus enlargement.

Despite the considerable scatter in results, it can be concluded that nucleation rates increase substantially with gas-phase water vapour content. The reasons for this effect have not been established. Whilst acceleration of chromia scaling and subsequently more severe alloy depletion have been suggested, direct observation in the case of Fe-20Cr at 650°C does not support this view. As seen in Fig. 10.24, the rate of chromia thickening is less in Ar-20CO₂-20H₂O than in oxygen, and substantially less than in Ar-20CO₂. It is possible also that water vapour promotes microcracking of the chromia scale [82].

The adverse effect of water vapour on the commencement of breakaway has also been suggested [27,76] as being due to an enhancement in the internal oxidation of chromium. This would decrease the availability of chromium at the alloy-scale interface for growth of more chromia when local scale failure led to an increase in oxygen activity. The hypothesis is that hydrogen penetrates the scale, dissolving in the substrate alloy and, through thermodynamic or kinetic interaction with solute oxygen, increasing the solubility or diffusivity of the latter. To date, there is no evidence available on this point.

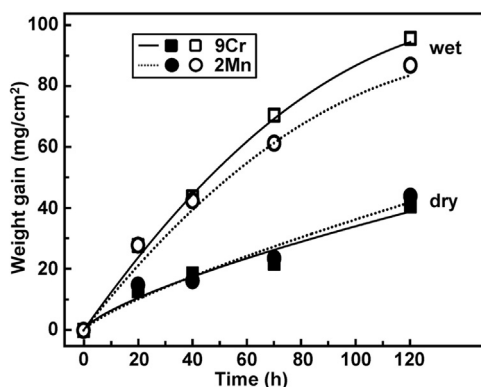


FIGURE 10.32 Reaction kinetics for Fe-9Cr and Fe-9Cr-2Mn in Ar-20CO₂ and Ar-20CO₂-20H₂O at 818°C. Reprinted from T.D. Nguyen, J. Zhang, D.J. Young, Corros. Sci. 89 (2014) 220, with permission from Elsevier.

The rate at which breakaway iron-rich oxide scales grow on Fe-9Cr is accelerated by the addition of water vapour to a CO₂ atmosphere [29], as seen in Fig. 10.32. Both outer and inner scale layers thicken more rapidly in the wet atmosphere (Fig. 10.33). Whilst the more rapid growth of the outer layer might be attributed to a changed boundary condition at the scale-gas interface, this presumably does not apply to the inner layer-outer layer interface, and the accelerated growth of the inner layer requires explanation.

As discussed in Section 10.5, gas-phase transport via the supposedly connected porosity of the inner layer is thought to be important. However, this process is dependent on the partial pressures of the participating gas species. A value of $p_{O_2} = 2 \times 10^{-19}$ atm is calculated from the Fe/FeO equilibrium at the scale-alloy interface, and molecular oxygen cannot provide any significant mass transfer within the pores. This corresponds via Eq. [10.2] to $p_{CO}/p_{CO_2} = 2$. No

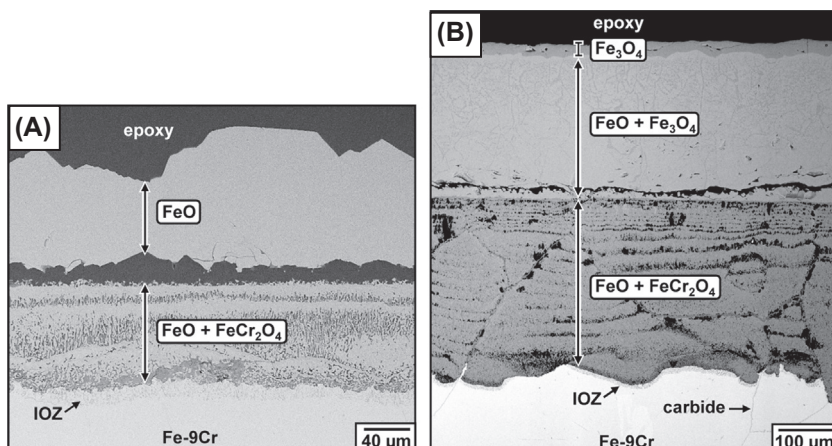


FIGURE 10.33 Reaction products on Fe-9Cr exposed for 70 h at 818°C (A) in Ar-20CO₂ and (B) in Ar-20CO₂-20H₂O. Reprinted from T.D. Nguyen, J. Zhang, D.J. Young, Corros. Sci. 89 (2014) 220, with permission from Elsevier.

elemental carbon is deposited, and Eq. [10.39] therefore requires $p_{\text{CO}} < 4.5 \text{ atm}$. Since the value of p_{CO} is limited to that of the gas phase, the effective maximum in this case is 0.2 atm and hence $p_{\text{CO}_2} < 0.1 \text{ atm}$ at the experimental temperature of 818°C . The value of $p_{\text{H}_2\text{O}}$ is limited simply by the gas-phase value of 0.2 atm. The maximum available partial pressures of CO_2 and H_2O are thus comparable, and would on this basis be expected to contribute similarly to gas-phase transport. The observed difference between rates in the two gases is more likely due to different permeation rates of the gas molecules in the outer, dense oxide layer.

Internal carburisation beneath iron-rich scales on Fe-Cr alloys and martensitic steels is decreased when water vapour is added to a CO_2 -rich atmosphere [8,21,76,83]. This is attributed to a decreased permeability of carbon through the iron-rich oxide, resulting in a lower carbon activity at the scale-alloy interface. Preferential uptake of an H-bearing species at internal sites where diffusion can occur, and partial exclusion of carbon have been suggested as the mechanism for this effect [21,22,76,84]. The suggestion is supported by the finding that H_2O is adsorbed preferentially over CO , at temperatures of $400\text{--}600^\circ\text{C}$, by a chromia scale grown on the pure metal [87].

In considering the effect of $\text{H}_2\text{O(g)}$ on internal carburisation, it is necessary to take into account not only the interactions between H_2O and CO_2 within the oxide, but also any changes to the scale phase constitution and/or morphology resulting from the presence of water vapour. As noted above, water vapour promotes formation of iron-rich oxide, which is more permeable to CO_2 than is the chromia scale frequently formed in dry gas.

Carburisation rates and corresponding carbide volume fractions formed in model alloys at 818°C in wet and dry CO_2 are listed in Table 10.6 [29]. The Fe-9Cr alloy fails to passivate in both gases, growing thick, iron-rich oxide scales which allow extensive internal carburisation. In the case of Fe-20Cr, water vapour promotes breakaway, leading to iron-rich nodule growth, whereas none form in dry CO_2 . The consequences for carburisation are profound, leading to much higher precipitate volume fractions and faster carbon

TABLE 10.6 Carburisation of Model Alloys in First 120 h of Reaction at 818°C in Ar-20 CO_2 and Ar-20 CO_2 -20 H_2O [29]

Alloy	Dry Gas		Wet Gas	
	f_v	Rate ($\text{cm}^2 \text{s}^{-1}$)	f_v	Rate ($\text{cm}^2 \text{s}^{-1}$)
Fe-9Cr	4.1×10^{-3}	$>3.6 \times 10^{-8}$	17.8×10^{-3}	$>1.9 \times 10^{-8}$
Fe-20Cr	4.6×10^{-6}	0.7×10^{-9}	2.7×10^{-3}	7.5×10^{-9}
Fe-20Cr-20Ni	2.9×10^{-4}	0.7×10^{-9}	0.2×10^{-4}	6.5×10^{-11}

penetration under the breakaway scales. This is a direct consequence of the greater carbon permeability of the iron oxide scales. Once significant carbide precipitation has occurred, repassivation becomes impossible, as the necessary chromium is immobilised as carbide.

Austenitic Fe-20Cr-20Ni failed to passivate in both wet and dry CO₂ gas mixtures, forming nodules of iron-rich oxide and undergoing carburisation. Rates of carbon entry into the alloy were slow, indicating the possible benefits of residual chromium-rich oxides in providing protection. In wet gas, Fe₂O₃ was formed, rather than the Fe₃O₄ grown in dry CO₂, and carburisation was decreased. This might indicate a lower carbon permeability in haematite.

10.6.5 Effects of SO₂ and O₂

Even at high temperatures, sulphur adsorbs strongly on many surfaces. It has long been known [86] that adsorbed sulphur can block carbon uptake by the substrate metal. In addition, carbon transmission through pure chromia scales is prevented by the addition of SO₂ to a CO/CO₂ gas mixture [87]. In the case of SO₂-bearing oxyfuel gas, the question then is whether protection against carburisation can be achieved without damage in the form of sulphidation. Preliminary work [75] has shown that corrosion in a simulated oxyfuel gas is faster than in CO₂ alone.

The addition of 0.5% SO₂ to Ar-50CO₂ doubled the rate of weight uptake by a P92 steel at 550°C [88]. This acceleration of corrosion was due to the formation of large islands of fast-growing FeS in the outer scale layer of magnetite, an effect attributed to the equilibrium



and the increase in p_{S_2} within the scale, where p_{O_2} is low (see Section 4.3). This deleterious effect was much reduced if 1% O₂ was also added to the gas. A simulated oxyfuel gas (Ar-25H₂O-60CO₂-3O₂-0.5SO₂) produced slightly more weight uptake than Ar-CO₂, but substantially less than Ar-CO₂-SO₂. The oxygen effect in reducing p_{S_2} is clear from Eq. [10.41], and the size of the effect is large.

Oxygen additions also have the effect of promoting the formation of protective chromium-rich oxide scales and reducing the extent of internal carburisation, as demonstrated for VM12 [89]. A more complex pattern of behaviour has been reported [90] for T92 steel in the temperature range 550–650°C. At a gas pressure of 1 atm, the addition of 1% O₂ to CO₂-30H₂O increases carburisation depths, but at $p_T = 80$ atm, the oxygen addition slows carburisation. This effect is not yet understood. Oxide scaling on this steel is also affected by oxygen, if sufficient is present. The addition of 1% O₂ to Ar-50CO₂ ($p_T = 1$ atm) has little effect on scaling at 550°C, but an addition of 3% slows the rate greatly, leading to the formation of protective chromium-rich

oxide over most of the alloy surface [27]. It is likely that preferential adsorption of molecular oxygen tends to exclude both H₂O and CO₂, thereby promoting chromium-rich oxide formation rather than iron oxide growth [91] and preventing carburisation. Comparison of the reaction product scales produced on P92 in simulated dry and wet oxyfuel environments showed that sulphur concentrations in the inner scale layer were much higher in dry gas [92], indicating again that the uptake of H₂O and SO₂ is a competitive process.

10.7 REMEDIAL MEASURES

The potentially disastrous consequences of CO₂ corrosion are deposition of elemental carbon (and disruption of the oxide scale), internal carburisation of the alloy (and degradation of its mechanical properties) and transition from protective oxide scaling to growth of iron-rich oxides (breakaway, leading to loss of metal section).

Carbon deposition is encountered at relatively low temperatures, where the exothermic nature of the Boudouard reaction leads it to produce high carbon activities. One solution is to lower the temperature still further so that the kinetics of the Boudouard reaction become too slow to pose a threat. This was the solution adopted for the early Magnox reactors, to protect the low alloy steel used in their heat exchangers. Of course, this derating of the reactors has a significant economic cost. A better solution is to use a higher alloy, martensitic steel (9–12% Cr) which provides a much more effective carbon sink, slowing the rate at which carbon activities rise within the scale.

An alternative approach is to use an alloy which can form a silica layer beneath a chromia scale. The silica appears to be impermeable to carbon. At the same time it is only slowly permeated by chromium, so that the oxygen activity at the chromia-silica interface rises. Even if CO₂ penetrates the chromia, the carbon activity resulting from equilibration with the elevated oxygen potential is low, and deposition can thereby be prevented.

At higher temperatures, carbon deposition becomes thermodynamically impossible, and the need is to resist carburisation and breakaway scaling. Austenitic and nickel-base heat-resisting alloys are more resistant to carburisation by virtue of their low carbon permeabilities. In combination with superior high-temperature strength, this makes these alloys attractive. However, research on their performance in CO₂ has only just begun.

Alumina-forming alloys have the potential to develop carbon-resistant scales. However, austenitic alumina formers do not succeed at the relatively low temperatures involved in CO₂ handling, as alloy diffusion is so slow. Ferritic alumina formers have potential, providing that adequate strength at service temperatures can be achieved. Oxide dispersion-strengthened alloys might find a role in such applications, as their resistance to CO₂ attack has recently been demonstrated [93]. Additional experimental information on the performance of these alloys in carbon dioxide is required.

Supercritical CO₂ poses a particularly severe problem because of the higher carbon activities achieved. The limited data available indicate that high alloy materials might resist carbon attack at modest temperatures, say 450°C, but attack is more severe at higher temperatures. It is likely that Ni-base alloys will be required in this situation.

Whilst understanding of the mechanism of CO₂ corrosion has advanced considerably, it must be conceded that more research is needed to obtain the necessary technological solutions.

REFERENCES

- [1] K. Hauffe, H. Pfeiffer, *Z. Metallk.* 44 (1953) 27.
- [2] F.S. Pettit, J.B. Wagner, *Acta Met.* 12 (1964) 35.
- [3] F.S. Pettit, R. Yinger, J.B. Wagner, *Acta Met.* 8 (1960) 617.
- [4] W.W. Smeltzer, *Trans. Met. Soc. AIME* 218 (1960) 674.
- [5] W.W. Smeltzer, *Acta Met.* 8 (1960) 377.
- [6] E.T. Turkdogan, W.M. McKewan, L. Zwell, *J. Phys. Chem.* 69 (1965) 327.
- [7] C.T. Fujii, R.A. Meussner, *J. Electrochem. Soc.* 114 (1967) 435.
- [8] T. Gheno, D. Monceau, D.J. Young, *Corros. Sci.* 64 (2012) 222.
- [9] T. Gheno, D. Monceau, D.J. Young, *Corros. Sci.* 77 (2013) 246.
- [10] J.E. Antill, A. Peakall, J.B. Warburton, *Corros. Sci.* 8 (1968) 689.
- [11] G.B. Gibbs, *Oxid. Met.* 7 (1973) 173.
- [12] G.B. Gibbs, M.R. Wootton, W.R. Price, K.E. Hodgson, *Oxid. Met.* 7 (1973) 185.
- [13] P.L. Harrison, R.B. Dooley, S.K. Lister, D.B. Meadowcroft, J.P. Noplan, R.E. Pendlebury, P.L. Surman, M.R. Wootton, in: *Proceedings BNES International Conference on Corrosion of Steels in CO₂* Reading University, 1974.
- [14] D.R. Holmes, R.B. Hill, L.M. Wyatt (Eds.), *BNES International Conference on Corrosion of Steels in CO₂*, Reading University, Reading, 1974.
- [15] C. Cabet, A. Terlain, P. Lett, L. Guétaz, J.M. Gentzbittel, *Mater. Corros.* 57 (2006) 147.
- [16] B.J.P. Buhre, L.K. Elliott, C.D. Sheng, R.P. Gupta, T.F. Wall, *Prog. Energy Combust. Sci.* 31 (2005) 283.
- [17] G. Cao, V. Firouzdor, K. Sridharan, M. Anderson, T.R. Allen, *Corros. Sci.* 60 (2012) 246.
- [18] K. Sridharan, *Corrosion in Supercritical Carbon Dioxide: Materials, Environmental Purity, Surface Treatment and Flow Issues*, US Department of Energy, Report No. 10-872 (2013).
- [19] V. Firouzdor, K. Sridharan, G. Cao, M. Anderson, T.R. Allen, *Corros. Sci.* 69 (2013) 281.
- [20] D. Goodison, R.J. Harris, *Br. J. Corros.* 4 (1969) 146.
- [21] T. Gheno, D. Monceau, J. Zhang, D.J. Young, *Corros. Sci.* 53 (2011) 2767.
- [22] J.P. Abellán, T. Olszewski, H.J. Penkalla, G.H. Meier, L. Singheiser, W.J. Quadakkers, *Mater. High Temp.* 26 (2009) 63.
- [23] C.S. Giggins, F.S. Pettit, *Oxid. Met.* 14 (1980) 363.
- [24] D.J. Young, P. Huczkowski, T. Olszewski, T. Hüttel, L. Singheiser, W.J. Quadakkers, *Corros. Sci.* 58 (2014) 161.
- [25] F. Rouillard, G. Molne, L. Martinelli, J.C. Ruiz, *Oxid. Met.* 77 (2012) 27.
- [26] F. Rouillard, G. Molne, M. Tabarant, J.C. Ruiz, *Oxid. Met.* 77 (2012) 57.
- [27] G.H. Meier, K. Jung, N. Mu, N.M. Yanar, F.S. Pettit, J.P. Abellán, T. Olszewski, L.N. Hierro, W.J. Quadakkers, G.R. Holcomb, *Oxid. Met.* 74 (2010) 319.
- [28] G.H. Meir, W.C. Coons, R.A. Perkins, *Oxid. Met.* 17 (1982) 235.

- [29] T.D. Nguyen, J. Zhang, D.J. Young, *Corros. Sci.* 89 (2014) 220.
- [30] M.G. Cox, B. McEnaney, V.D. Scott, *Philos. Mag.* 26 (1972) 839.
- [31] T.D. Nguyen, J. Zhang, D.J. Young, *Corros. Sci.* 100 (2015) 448.
- [32] M. Haensel, C.A. Boddington, D.J. Young, *Corros. Sci.* 45 (2003) 967.
- [33] M.R. Taylor, J.M. Calvert, D.G. Lees, D.B. Meadowcroft, *Oxid. Met.* 14 (1980) 499.
- [34] T.D. Nguyen, J. Zhang, D.J. Young, *Scripta Mater.* 69 (2013) 9.
- [35] P. Promdirek, G. Lothongkum, S. Chandra-Ambhorn, A.G.Y. Wouters, *Oxid. Met.* 81 (2014) 315.
- [36] H.E. McCoy, *Corrosion* 21 (1965) 84.
- [37] W.B. Jepson, J.E. Antill, J.B. Warburton, *Br. Corros. J.* 1 (1965) 15.
- [38] R.A. Holm, H.E. Evans, *Werkst. Korros.* 38 (1987) 115.
- [39] T.D. Nguyen, J. Zhang, D.J. Young, *Corros. Sci.* 76 (2013) 231.
- [40] T.A. Ramanarayanan, R. Ayer, R. Petkovic-Luton, D.P. Leta, *Oxid. Met.* 29 (1988) 445.
- [41] A.M. Pritchard, A.E. Truswell, in: *Proceedings of BNES International Conference on Corrosion of Steels in CO₂*, Reading University, Reading, 1974.
- [42] F. Rouillard, F. Charton, G. Moine, in: *Corrosion Behaviour of Different Metallic Materials in Supercritical CO₂ at 550°C and 250 Bar, SC CO₂ Power Cycle Symposium*, 2009.
- [43] T. Furukawa, Y. Inagaki, M. Aritomi, *J. Power Energy Syst.* 4 (2010) 252.
- [44] L.-F. He, P. Roman, B. Leng, K. Sridharan, M. Anderson, T.R. Allen, *Corros. Sci.* 82 (2014) 67.
- [45] I. Wolf, H.J. Grabke, *Solid State Commun.* 54 (1985) 5.
- [46] A.D. Pelton, H. Schmalzried, J. Sticher, *J. Phys. Chem. Solids* 40 (1979) 1103.
- [47] H. Davies, A. Dinsdale, *Mater. High Temp.* 22 (2005) 15.
- [48] B. Sundman, B. Jansson, J.O. Andersson, *CALPHAD: Comput. Coupling Phase Diag. Thermochem.* 9 (1985) 153.
- [49] A.W. Bowen, G.M. Leak, *Met. Trans.* 1 (1970) 1695.
- [50] C. Wagner, *Zeits. Elektrochem.* 63 (1959) 772.
- [51] E. Budke, C. Herzig, H. Wever, *Phys. Stat. Sol.* 127 (1991) 87.
- [52] E.K. Ohriner, J.E. Morral, *Scripta Met.* 13 (1979) 7.
- [53] The T91/P91 Book, Vallourec and Mannesmann Tubes, 1999.
- [54] K.F. McCartney, D.R. Boehme, *J. Solid State Chem.* 79 (1989) 19.
- [55] C. Wagner, *J. Electrochem. Soc.* 99 (1952) 369.
- [56] J. Crank, *The Mathematics of Diffusion*, Oxford University Press, Oxford, 1975.
- [57] D.P. Whittle, *Oxid. Met.* 4 (1972) 171.
- [58] J. Topfer, S. Aggarwal, R. Dieckmann, *Solid State Ionics* 81 (1995) 251.
- [59] R.A. Rapp, *Acta Metall.* 9 (1961) 730.
- [60] D.J. Young, T.D. Nguyen, P. Felfer, J. Zhang, J.M. Cairney, *Scripta Mater.* 77 (2014) 29.
- [61] S.C. Tsai, A.M. Huntz, C. Dolin, *Mater. Sci. Eng. A* 212 (1996) 6.
- [62] J. Zurek, D.J. Young, E. Essuman, M. Hänsel, H.J. Penkalla, L. Niewolak, W.J. Quadakkers, *Mater. Sci. Eng. A* 477 (2008) 259.
- [63] A. Kumar, D.L. Douglass, *Oxid. Met.* 10 (1976) 1.
- [64] H.E. Evans, D.A. Hilton, R.A. Holm, S.J. Webster, *Oxid. Met.* 19 (1983) 1.
- [65] M.J. Bennett, J.A. Desport, P.A. Labun, *Oxid. Met.* 22 (1984) 291.
- [66] F.H. Stott, G.J. Gabriel, F.I. Wei, G.C. Wood, *Mater. Corros.* 38 (1987) 521.
- [67] T.D. Nguyen, J. Zhang, D.J. Young, *Oxid. Met.* 81 (2014) 549.
- [68] H. Li, J. Zhang, D.J. Young, *Corros. Sci.* 54 (2012) 127.
- [69] H.J. Grabke, E.M. Muller-Lorenz, in: *Corrosion 2001*, NACE International, 2001 p. Paper 01373.
- [70] D.L. Douglass, J.S. Armijo, *Oxid. Met.* 2 (1970) 207.

- [71] L. Niewolak, D.J. Young, H. Hattendorf, L. Singheiser, W.J. Quadakkers, *Oxid. Met.* 82 (2014) 123.
- [72] D.R. Holmes, R.B. Hill, L.M. Wyatt, in: Proceedings of BNES International Conference on Corrosion of Steels in CO₂, Reading University, Reading, 1974.
- [73] B. Vitalis, in: 5th International Conference on Advances in Materials Technology for Fossil Power Plants, Marco Island, Florida, USA, 2007 (Paper T).
- [74] B. Bordinet, *Mater. Corros.* 59 (2008) 361.
- [75] B.S. Covino, S.A. Matthes, S.J. Bullard, in: Corrosion 2008, NACE International, 2008. Paper 08456.
- [76] N. Mu, K.Y. Jung, N.M. Yanar, G.H. Meier, F.S. Pettit, G.R. Holcomb, *Oxid. Met.* 78 (2012) 221.
- [77] J.P. Abellan, T. Olszewski, G.H. Meier, L. Singheiser, W.J. Quadakkers, *Inter. J. Mater. Res.* 101 (2010) 287.
- [78] T. Gheno, H. Li, J. Zhang, D.J. Young, *Mater. Sci. Forum* 654–656 (2010) 1948.
- [79] M.G. Cox, B. McEnaney, V.D. Scott, *Philos. Mag.* 29 (1974) 585.
- [80] C. Leygraf, G. Hultquist, *Surf. Sci.* 61 (1976) 69.
- [81] U.R. Evans, *Trans. Faraday Soc.* 41 (1945) 365.
- [82] Y. Ikeda, K. Nii, *Trans. Natl. Res. Inst. Met.* 26 (1984) 52.
- [83] W.J. Quadakkers, T. Olszewski, J.P. Abellan, V. Shemet, L. Singheiser, *Mater. Sci. Forum* 696 (2011) 194.
- [84] D.J. Young, *Int. J. Hydrogen Energy* 32 (2007) 3763.
- [85] C. Enghel, E. Hornlund, G. Hultquist, M. Limback, *Appl. Surf. Sci.* 233 (2004) 392.
- [86] H.J. Grabke, E.M. Petersen, S.R. Srinivasan, *Surf. Sci.* 67 (1977) 501.
- [87] X.G. Zheng, D.J. Young, *Corros. Sci.* 38 (1996) 1877.
- [88] P. Huczkowski, T. Olszewski, M. Schiek, B. Lutz, G.R. Holcomb, V. Shemet, W. Nowak, G.H. Meier, L. Singheiser, W.J. Quadakkers, *Mater. Corros.* 65 (2014) 121.
- [89] W.J. Quadakkers, T. Olszewski, J.P. Abellan, L. Singheiser, *VDI-Berichte* 2012 (2010) 81.
- [90] D. Huener, A. Kranzmann, *Corros. Sci.* 53 (2011) 2306.
- [91] J. Ehlers, D.J. Young, E.J. Smaardyk, A.K. Tyagi, J. Penkalla, L. Singheiser, W.J. Quadakkers, *Corros. Sci.* 48 (2006) 3428.
- [92] K. Chandra, A. Kranzmann, R. Saliwan Neumann, F. Rizzo, *Oxid. Met.* 84 (2015) 463.
- [93] V. Firouzdor, G.P. Gao, K. Sridharan, M. Anderson, T.R. Allen, *Mater. Corros.* 66 (2015) 137.